J. Fluid Mech. (2014), *vol.* 743, *pp.* 327–357. © Cambridge University Press 2014
doi:10.1017/jfm.2014.31

Viscid–inviscid pseudo-resonance in streamwise corner flow

Oliver T. Schmidt† and Ulrich Rist

Institut für Aerodynamik und Gasdynamik, Universität Stuttgart, Pfaffenwaldring 21, 70569 Stuttgart, Germany

(Received 15 October 2012; revised 18 December 2013; accepted 10 January 2014; first published online 4 March 2014)

The stability of streamwise corner flow is investigated by means of direct numerical simulation at subcritical Reynolds numbers. The flow is harmonically forced, and global modes are extracted through a spectral decomposition. Spatial amplification in the near-corner region is observed even though the flow is shown to be subcritical in terms of spatial linear theory. This apparent discrepancy is resolved by extending the local analysis to include non-modal effects. It is demonstrated that the amplification is a result of the interaction between two coexistent spatial transient growth processes that can be associated with different parts of the linear stability spectrum. A detailed investigation of the underlying mechanisms shows that the transient amplification behaviour is caused by pseudo-resonance between the inviscid corner mode, and different sets of viscous modes. By comparison with studies of other locally inflectional flows, it is found that viscid–inviscid pseudo-resonance might be a general phenomenon leading to selective noise amplification.

Key words: Compressible boundary layers, Absolute/convective instability, Boundary layer stability

1. Introduction

The viscous flow in a right-angled streamwise-aligned corner has been the focus of numerous experimental and theoretical studies for over 60 years due to its significance in many technical applications, especially in aeronautical engineering. Wing–body junctions on airplanes and the corner regions in wind tunnels are prominent examples.

Most generically, the corner flow problem is modelled as two perpendicular semi-infinite flat plates with the streamwise coordinate x along the intersection line and the coordinates y and z spanning the transverse plane, as depicted in figure 1. The superposition of the displacement effects of the two adjacent walls induces a highly three-dimensional secondary flow field that decays algebraically with distance from the opposing wall. The appropriate far-field boundary conditions are usually found by means of asymptotic perturbation theory.

Early work on the subject was conducted by Carrier (1947). A major milestone was the work by Rubin (1966), who derived the so-called corner flow equations that govern the self-similar laminar viscous corner flow problem using the method of

† Email address for correspondence: o.schmidt@iag.uni-stuttgart.de

https://doi.org/10.1017/jfm.2014.31 Published online by Cambridge University Press

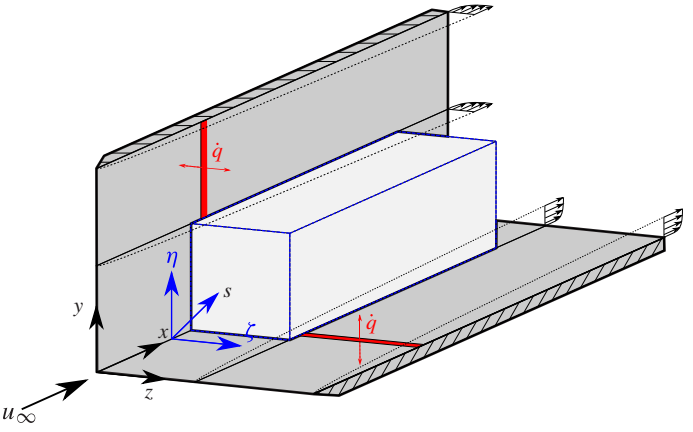


FIGURE 1. Sketch of the flow in an axial corner. Blue lines represent the computational domain for the direct numerical simulation of § 4. The origin of the Cartesian coordinate system (x, y, z) is located at the intersection point of the plates on the leading edge; u_∞ is the potential free-stream velocity; (η, ζ) is the alternative self-similar coordinate frame used in the local analyses of §§ 3 and 5; and s is the coordinate along the corner bisector, i.e. $y = z$. The harmonic forcing induced in the form of a heat flux by the heating strips (red bands) is denoted by $\dot{q}$.

matched asymptotic expansions. A numerical solution was first presented by Rubin & Grossman (1971). In the latter, the authors relied on the work of Pal & Rubin (1971) on asymptotic behaviour for the far-field boundary conditions. A remarkable feature of the corner flow equations was found three decades later by Ridha (1992) in his study of non-zero pressure gradient solutions. The equations exhibit dual solutions distinguished by different wall shear, one of which can be identified as equivalent to the classical Blasius boundary-layer solution and was the only solution studied previously. The compressibility effect was introduced into the problem by Weinberg & Rubin (1972) for a unity Prandtl number model fluid. Later, Mikhail & Ghia (1978) extended the equations to general compressible fluids. Different other aspects have been in the focus, such as variable corner angles (Barclay & Ridha 1980), wall suction (Barclay & El-Gamal 1983, 1984), forced and free convection (Ridha 2002), as well as non-similarity solutions due to a more general form of the pressure gradient (Duck, Stow & Dhanak 1999).

Most experimental work on the subject dates back to the 1970s and 1980s, most notably the work by Zamir & Young (1970), Barclay (1973), El-Gamal & Barclay (1978), Zamir & Young (1979), Zamir (1981) and Kornilov & Kharitonov (1982), and before that period by Nomura (1962). Two key observations were made throughout the experiments. First, the laminar mean flow deviates from the self-similar solution in the near-corner region at some distance from the leading edge in the form of an outward bulge in the lines of constant streamwise velocity. Second, laminar–turbulent transition occurs much earlier than for the flat-plate scenario, even at small favourable streamwise pressure gradients. A connection with the first-mentioned velocity isoline deformation and early transition suggests itself. Kornilov & Kharitonov (1982) argued that the deformation develops under the influence of a local pressure gradient in the intersection region along the leading edge. A practically streamwise pressure gradientless flow was achieved by the authors with a specifically designed

https://doi.org/10.1017/jfm.2014.31 Published online by Cambridge University Press

leading-edge geometry. The realised flow did not exhibit the deformation and closely resembled the theoretical self-similar solution.

However, there still exists an unresolved discrepancy between experimental findings and theoretical results, which consistently predict a much higher critical Reynolds number. Traditionally, the critical Reynolds number is determined by means of a linear stability analysis, i.e. the amplification behaviour of wave-like perturbations of infinitesimally small amplitude superimposed onto the steady base state. Here, *critical* refers to the point in parameter space where neutral stability first occurs. As a classical boundary-layer-type flow, the corner problem falls into the category of convectively unstable flows, meaning that perturbations are constantly convected downstream. Hence, the flow acts as a spatial amplifier of incoming perturbations with no intrinsic dynamics, as opposed to absolutely unstable flows where initial disturbances are amplified exponentially everywhere within the laboratory frame (see e.g. Chomaz 2005). The first stability studies of Lakin & Hussaini (1984), Dhanak (1992, 1993) and Dhanak & Duck (1997) were restricted to the one-dimensional blending boundary-layer profile between the corner region and the asymptotic far field. Two-dimensional local stability calculations of the transverse plane were first conducted by Balachandar & Malik (1995) for the inviscid problem. Analyses of the viscous problem by Lin, Wang & Malik (1996) and Parker & Balachandar (1999) followed. The spatial stability problem was addressed by Galionis & Hall (2005) through solution of the parabolised stability equations. Compressibility was taken into account in a similar study by Schmidt & Rist (2011).

The aforementioned inviscid stability study by Balachandar & Malik (1995) revealed an inviscid instability in the direct corner region due to the locally inflectional nature of the streamwise velocity profile along the corner bisector. Their study of the stability properties of the one-dimensional bisector profile implied a two orders of magnitude lower critical Reynolds number as compared to the flat-plate scenario, where viscous instability sets in at $Re_{x,crit} \approx 9 \times 10^4$. However, none of the more general two-dimensional stability studies conducted thereafter confirmed the findings, even though the inviscid mechanism is recovered in the form of the so-called *corner mode*, consistently identified in the spectrum of the viscous linear stability operator. The neutral stability values for the corner mode differ drastically between different studies, indicating a high sensitivity with respect to the numerical scheme and/or far-field boundary treatment. Parker & Balachandar (1999) noted that no unstable inviscid modes were observed for $Re_{x,crit} \lesssim 5 \times 10^5$, while Galionis & Hall (2005) and Schmidt & Rist (2011) found the onset of inviscid instability to occur slightly above the viscous stability limit. In two recent studies, Alizard, Robinet & Rist (2010) and Alizard, Robinet & Guiho (2013) addressed the sensitivity to base-flow variations and transient growth of (optimal) perturbations. The authors found that even small base-flow variations can lead to a significant reduction of the critical Reynolds number and, in the latter citation, that corner flow is prone to rapid transient growth through the Orr mechanism and the lift-up effect, given a suitable initial condition.

Despite all efforts, the question of the cause of the rapid transition observed in experiment has not yet been answered with certainty. Different routes to turbulence are generally possible for wall-bounded shear-flow configurations, as charted in the well-known review by Morkovin, Reshotko & Herbert (1994). According to the author, laminar–turbulent transition can be categorised into five scenarios after environmental disturbances are translated into shear-layer instabilities by some receptivity mechanism. For low-amplitude perturbations, exponential eigenmode (in accordance with linear stability theory) or algebraic non-modal growth can be expected. Alternatively, modal

https://doi.org/10.1017/jfm.2014.31 Published online by Cambridge University Press

or non-modal growth can be bypassed in high-amplitude disturbance environments leading directly to transition through nonlinear interaction. Combinations of the different mechanisms produce the five paths to transition suggested. It is currently not clear which scenario applies to streamwise corner flow.

The study at hand is motivated by the discrepancies between theoretical predictions and experimental observations. We are focusing on the subcritical flow response to low-amplitude harmonic forcing by deploying local spatial linear stability theory (§ 3) and direct numerical simulation (§ 4) of the fully non-parallel problem without model assumptions. The results are compared with the aid of a spectral decomposition of the simulation data. At first glance, the results are found to be in disagreement. However, the apparent discrepancy is resolved by an extended non-modal analysis of the underlying spatial stability operator in § 5. It is demonstrated that spatial transient growth caused by pseudo-resonance between viscous modes and the inviscid corner mode explains the subcritical amplification behaviour observed in simulations. A discussion of the results including indications for transition behaviour are given in § 6. In the following § 2, the reader is introduced to the governing equations, the base state formulation and the numerical framework.

2. Governing equations, base state and numerical methods

This section is subdivided as follows: the starting point is the compressible Navier–Stokes equations introduced in § 2.1. A steady laminar base state is calculated as a solution to a simplified set of equations, and with the aid of asymptotic boundary conditions in § 2.2. The solution methodology for the full set of equations used to compute the response of the base flow to harmonic forcing, i.e. direct numerical simulation (DNS), is presented in § 2.3. Section 2.6 introduces the spectral decomposition method used to reobtain modal information to compare DNS results to solutions of the spatial local linear stability problem calculated as shown in § 2.4. The short-time/distance response of a flow to forcing may differ from results obtained by the eigenvalue-based linear stability approach. This behaviour is governed by non-modal theory to be described in § 2.5.

2.1. *Navier–Stokes equations for a compressible ideal gas*

The flow of a compressible ideal gas is most generally governed by the three-dimensional Navier–Stokes equations (NSE) consisting of the continuity equation (2.1*a*), the momentum equation (2.1*b*) and the energy equation (2.1*c*):

$$\frac{\partial \rho}{\partial t} = -\boldsymbol{\nabla}\cdot\rho\boldsymbol{u}, \tag{2.1a}$$

$$\frac{\partial \rho\boldsymbol{u}}{\partial t} = -\frac{1}{2}\boldsymbol{\nabla}\cdot(\boldsymbol{u}\otimes\rho\boldsymbol{u}+\rho\boldsymbol{u}\otimes\boldsymbol{u}) - \boldsymbol{\nabla}p + \frac{1}{Re}\boldsymbol{\nabla}\cdot\boldsymbol{\tau}, \tag{2.1b}$$

$$\frac{\partial \rho e}{\partial t} = -\boldsymbol{\nabla}\cdot\rho e\boldsymbol{u} + \frac{1}{(\gamma-1)RePrMa_\infty^2}\boldsymbol{\nabla}\cdot k\boldsymbol{\nabla}T - \boldsymbol{\nabla}\cdot p\boldsymbol{u} + \frac{1}{Re}\boldsymbol{\nabla}\cdot\boldsymbol{\tau}\boldsymbol{u}. \tag{2.1c}$$

Here, ρ is the density, $\boldsymbol{u}=(u, v, w)^{\mathrm{T}}$ the velocity in the Cartesian coordinate frame $\boldsymbol{x}=(x, y, z)^{\mathrm{T}}$, p the pressure, T the temperature and e the total energy. The dynamic viscosity μ and the thermal conductivity k are material properties. The pressure is non-dimensionalised by twice the dynamic pressure $\rho_\infty^* u_\infty^{*2}$, the x, y, z coordinates by the local displacement thickness $\delta_1^* = \int_0^\infty [1-\rho^* u^*/\rho_\infty^* u_\infty^*]\,\mathrm{d}y^*$ and all other quantities by

https://doi.org/10.1017/jfm.2014.31 Published online by Cambridge University Press

Ma	Pr	γ	p^*_∞ (hPa)	T^*_∞ (K)	c^*_p (J kg^{-1} K^{-1})	R^* (J kg^{-1} K^{-1})
0.8	0.714	1.4	1013.25	293.15	1005	287

TABLE 1. Dimensionless quantities and free-stream properties.

their respective dimensional free-stream value. Superscript $*$ and subscript ∞ denote dimensional quantities and free-stream values, respectively. The viscous stresses in a Newtonian fluid are given by

$$\boldsymbol{\tau} = \mu(\boldsymbol{\nabla u} + \boldsymbol{\nabla u}^{\mathrm{T}}) + \lambda(\boldsymbol{\nabla}\cdot\boldsymbol{u})\boldsymbol{I}, \quad \lambda = -\frac{2}{3}\mu, \tag{2.2a,b}$$

where the Stokes hypothesis (2.2*b*) simplifies the expression by relating the bulk viscosity λ to the dynamic viscosity. The temperature can be calculated from the definition of the total energy (2.3*a*). The system of equations (2.1) is closed by relating the pressure to the density and temperature through the ideal gas law (2.3*b*):

$$T = \gamma(\gamma-1)Ma^2_\infty\left(e - \frac{1}{2}\boldsymbol{u}\cdot\boldsymbol{u}\right), \quad p = \frac{1}{\gamma Ma^2_\infty}\rho T. \tag{2.3a,b}$$

Here, γ is the heat capacity ratio and Ma_∞ the free-stream Mach number. The Mach number Ma, Reynolds number Re and Prandtl number Pr,

$$Re = \frac{\rho^*_\infty u^*_\infty \delta^*_1}{\mu^*_\infty}, \quad Pr = \frac{c^*_p \mu^*_\infty}{k^*_\infty}, \quad Ma = \frac{u^*_\infty}{a^*_\infty}, \tag{2.4a,b,c}$$

describe the ratio of inertial to viscous forces, the ratio of momentum to thermal diffusivity and the effect of compressibility, respectively.

2.2. *Base state*

A steady corner flow base state is calculated as a solution to the parabolised Navier–Stokes equations (PNS). The latter are obtained most conveniently by omitting the unsteady terms, the streamwise pressure gradient and all viscous terms containing partial derivatives with respect to the streamwise direction from (2.1). The underlying assumptions are justified for boundary-layer-type flows without a streamwise pressure gradient (Rubin & Tannehill 1992; Tannehill, Anderson & Pletcher 1997). The parabolised set of equations is solved by a Chebyshev–Chebyshev collocation method in combination with implicit space marching as described in Schmidt & Rist (2011) for the fluid properties listed in table 1. The reader is referred to the same paper for a validation by comparison with the literature for Mach numbers up to 1.5 and details on boundary conditions.

The ideal gas constant R^* appears in the dimensional version of (2.3*b*), i.e. $p^* = \rho^* R^* T^*$. Sutherland's law

$$\left.\begin{aligned} &\mu^*(T) = \mu^*_{ref} T^{3/2}\frac{1+T_s}{T+T_s}, \\ &\text{where} \quad \mu^*_{ref}(T^*_{ref} = 280\ \mathrm{K}) = 1.735\times10^{-5}\ \mathrm{kg\ m\ s^{-1}} \quad \text{and} \quad T_s = \frac{110.4\ \mathrm{K}}{T^*_\infty}, \end{aligned}\right\} \tag{2.5}$$

https://doi.org/10.1017/jfm.2014.31 Published online by Cambridge University Press

empirically connects the dynamic viscosity to the temperature using a dimensional reference viscosity μ^*_{ref} and a non-dimensional reference temperature T_s. By introducing a self-similarity coordinate frame $\boldsymbol{\eta} = (\eta, \zeta)^{\mathrm{T}}$ with

$$\eta = \frac{\sqrt{2Re_x}}{2x^*} y^*, \quad \zeta = \frac{\sqrt{2Re_x}}{2x^*} z^*, \tag{2.6}$$

and the cross-flow velocity scaling law

$$v(\boldsymbol{\eta}) = \frac{\beta}{\sqrt{2Re_x}} v(\boldsymbol{x}^*), \quad w(\boldsymbol{\eta}) = \frac{\beta}{\sqrt{2Re_x}} w(\boldsymbol{x}^*), \tag{2.7}$$

the dependence of the solution on the streamwise coordinate is removed. Here $Re_x = \rho^*_\infty u^*_\infty x^*/\mu^*_\infty$ is the Reynolds number based on the dimensional streamwise position and $\beta = \int_0^\infty [1 - u/T]\,\mathrm{d}\eta$ is the displacement-thickness-related quantity as defined by Ghia & Davis (1974). In the latter citation, the authors provide the momentum equation

$$\left.\begin{gathered} \mu_0 \frac{\mathrm{d}^2 w_1}{\mathrm{d}\eta^2} + \left[\frac{\mathrm{d}\mu_0}{\mathrm{d}\eta} + \rho_0(\eta u_0 - v_1)\right] \frac{\mathrm{d}w_1}{\mathrm{d}\eta} + \rho_0 u_0 w_1 = \beta, \\ \text{with } w_1(0) = 0 \quad \text{and} \quad w_1(\eta \to \infty) = \beta, \end{gathered}\right\} \tag{2.8}$$

that governs the first-order asymptotic cross-flow $w_1(\eta, \zeta \to \infty)$. The zeroth-order quantities denoted by subscript 0 resemble the classical compressible flat-plate boundary-layer solution. The solution to (2.8) is enforced on the far-field boundaries and corresponds to the lower branch solution in the work of Ridha (1992). The temporal stability results for the upper and lower branch solutions were found to differ very little by Parker & Balachandar (1999) for a zero streamwise pressure gradient. The parabolised stability equation-based approach for the spatial linear problem by Galionis & Hall (2005) attested a slightly lower critical Reynolds number to the lower branch solution but found the upper branch counterpart to be more sensitive with respect to changes of the adverse pressure gradient. Apart from the study at hand, the lower branch solution was also utilised in the more recent sensitivity study by Alizard *et al.* (2010).

Using the procedure described above, a self-similar solution is converged by integration in the parabolised coordinate direction. The converged solution can be rescaled to any desired streamwise position subsequently. Just as for the closely related flat-plate boundary-layer scenario, the solution becomes singular at the leading edge and is therefore not valid in that region. The self-similar solution is preferred over the PNS solution to allow for comparison with other authors. The differences are, however, negligible. Figure 2 shows the base flow computed as described above. The negative values of v in figure 2(*b*) close to the vertical wall at $z = 0$ indicate a wall jet that pulls fluid towards the corner that is subsequently pushed out of the domain along the corner bisector. The curvature of the bisector streamwise velocity profile depicted in figure 2(*c*) reveals an inflexion point, suggesting the possibility of an inviscid instability according to Rayleigh's theorem.

2.3. *Direct numerical simulations*

The evolution of a perturbation upon the steady base-flow solution from § 2.2 is simulated by solving the full set of governing equations (2.1), i.e. direct numerical

https://doi.org/10.1017/jfm.2014.31 Published online by Cambridge University Press

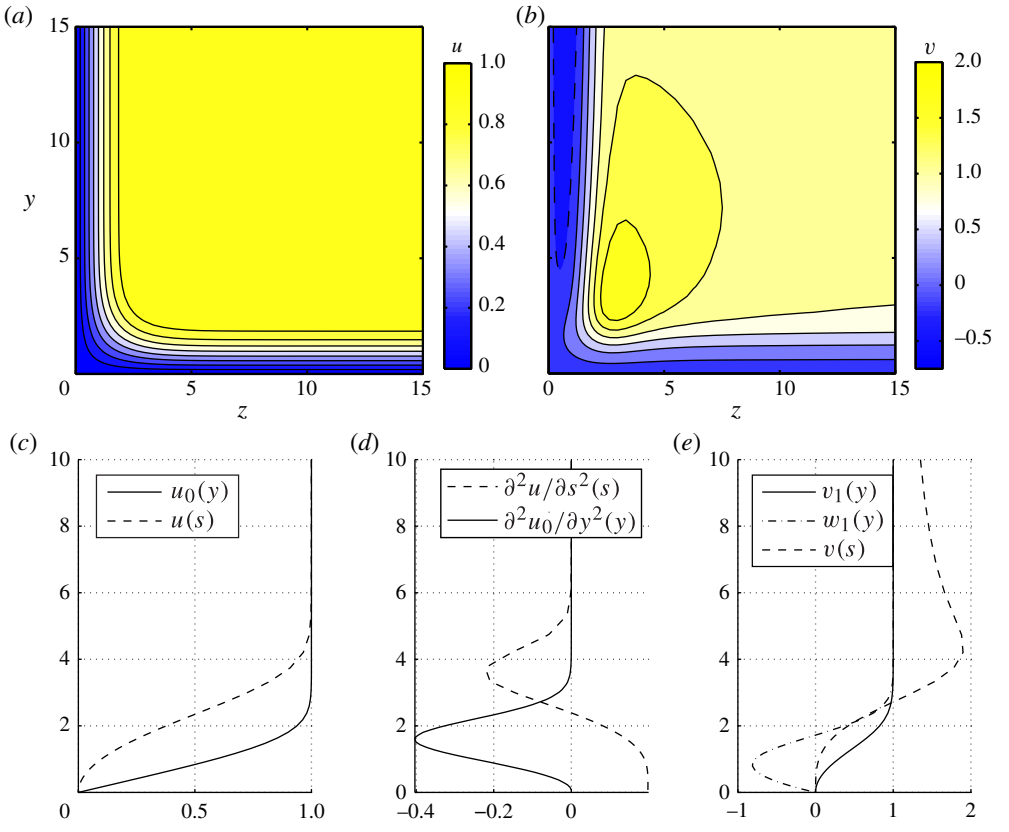


FIGURE 2. Steady base flow for the DNS: (*a*) streamwise velocity u; (*b*) y component v of the cross-flow velocity field; (*c*) streamwise bisector $u(s)$ and asymptotic velocity profiles $u_0(y)$; (*d*) curvature of $u(s)$ and $u_0(y)$; and (*e*) bisector $v(s) = w(s)$ and asymptotic $v_1(y)$, $w_1(y)$ cross-flow velocity profiles.

simulation. The spatial discretisation of the computational domain Ω is based on a sixth-order accurate compact finite difference scheme, which is stabilised by alternating up- and downwind biasing as suggested by Kloker (1997). For time integration, a standard fourth-order accurate Runge–Kutta method is employed. A detailed description of the NS3D code can be found in Babucke (2009). The code is validated by comparison with linear theory and turbulence statistics in wall-bounded and free shear-layer flows. Prior to this, it was applied in the study of noise generation in a plane mixing layer by Babucke, Kloker & Rist (2008).

The asymptotic nature of the base flow in combination with perturbations that are active over the entire spanwise domain extent permits the use of standard boundary conditions on the far field. We therefore rely on a perturbation formulation that allows us to impose boundary conditions solely on the perturbation flow field while keeping the base state constant (see e.g. Rist & Fasel 1995). Traditionally, the flow field is Reynolds decomposed into a steady base state $\boldsymbol{q}_0(\boldsymbol{x})$ and a time-varying perturbation part $\boldsymbol{q}'(\boldsymbol{x}, t)$ as

$$\boldsymbol{q}(\boldsymbol{x}, t) = \boldsymbol{q}_0(\boldsymbol{x}) + \boldsymbol{q}'(\boldsymbol{x}, t). \tag{2.9}$$

https://doi.org/10.1017/jfm.2014.31 Published online by Cambridge University Press

x_0	Re_0	x_1	Re_1	$x_{p,0}$	$x_{p,1}$	$y_1,\ z_1$	N_x	$N_y,\ N_z$	Δt
79.89	312.95	303.57	610.04	86.61	100.06	50	500	250	0.0195

TABLE 2. Computational domain for the DNS: subscripts 0 and 1 denote start and end; $N_{x,y,z}$ is the number of grid points in the respective direction; and $x_{p,0}$ and $x_{p,1}$ delimit the streamwise perturbation strip in (2.16).

Here, $\boldsymbol{q} = (\rho, \rho u, \rho v, \rho w, e)^{\mathrm{T}}$ is the solution vector of conservative variables to (2.1). The perturbation formulation of the Navier–Stokes equations is found by inserting ansatz (2.9) into (2.1). Under the assumption that $\boldsymbol{q}_0(\boldsymbol{x})$ satisfies (2.1) for itself, all terms consisting of base-flow derivatives only vanish, leaving a set of evolution equations for $\boldsymbol{q}'(\boldsymbol{x}, t)$. We use an alternative strategy that allows us to impose boundary conditions on the perturbation field with minimal code modification, i.e. just by adding a source term to (2.1) instead of implementing the perturbation equations. Consider the equivalent operator notation form

$$\frac{\partial \boldsymbol{q}}{\partial t} = \mathscr{NS}(\boldsymbol{q}) \tag{2.10}$$

of (2.1*a*). By introducing ansatz (2.9) into (2.10), noting that $\mathscr{NS}(\boldsymbol{q}) = \mathscr{NS}(\boldsymbol{q}_0 + \boldsymbol{q}')$, splitting the time derivative and rearranging, we obtain

$$\frac{\partial \boldsymbol{q}'}{\partial t} = \mathscr{NS}(\boldsymbol{q}) - \frac{\partial \boldsymbol{q}_0}{\partial t}. \tag{2.11}$$

From (2.11), any solver for (2.1) can be converted to an equivalent perturbation formulation by adding $-\partial \boldsymbol{q}_0/\partial t$ as a source term. Conveniently, the latter temporal derivative of the base flow has to be computed only once by the same algorithm at the beginning of the simulation if the time step Δt is kept constant. Note that the assumption that $\boldsymbol{q}_0(\boldsymbol{x})$ is a solution to (2.1) can be dropped in this context without any loss of generality, yielding an even more flexible computational method in comparison to a dedicated perturbation formulation solver. For the case at hand, $\partial \boldsymbol{q}_0/\partial t$ was found to be small and most likely caused by the different differentiation schemes and the underlying assumptions of the PNS method. Hence, it is concluded that the self-similar base state is a good approximation to a full Navier–Stokes solution.

2.3.1. *Computational domain and boundary conditions*

Details about the computational domain extent and resolution are listed in table 2. The streamwise extent corresponds to a Reynolds-number regime of $2.5 \times 10^4 \leqslant Re_x \leqslant 9 \times 10^4$. Note that this is below the critical Reynolds number of $Re_{crit} \approx 9 \times 10^4$ found from linear stability theory. The displacement thickness $\delta_1^*(x_0) = 1.7528 \times 10^{-5}$ m at the inlet is used for non-dimensionalisation of the coordinates. A total of 65 grid points are concentrated in the near-wall regions $y < 6$ and $z < 6$, while the rest are equidistantly distributed in the far field. Grid independence of the solutions was confirmed by comparison with higher resolved test calculations.

Adiabatic no-slip wall boundary conditions are enforced on both walls, i.e.

$$\boldsymbol{u}' = 0, \quad \frac{\partial T'}{\partial \boldsymbol{n}} = 0 \quad \text{on } (x, y = 0, z) \text{ and } (x, y, z = 0), \tag{2.12}$$

https://doi.org/10.1017/jfm.2014.31 Published online by Cambridge University Press

where $\boldsymbol{n}$ denotes the respective boundary normal direction. The pressure is extrapolated from the interior field and the density is calculated from the ideal gas law (2.3*b*). On the inlet and both far-field boundaries, homogeneous Neumann conditions

$$\frac{\partial \boldsymbol{q}'}{\partial \boldsymbol{n}} = 0 \quad \text{on } (x, y = y_1, z), \ \ (x, y, z = z_1) \text{ and } (x = x_0, y, z) \tag{2.13}$$

are applied. The outlet is treated by a subsonic outflow condition

$$\left.\frac{\partial \boldsymbol{q}'}{\partial t}\right|_N = \left.\frac{\partial \boldsymbol{q}'}{\partial t}\right|_{N-1} \quad \text{on } (x = x_1, y, z), \tag{2.14}$$

which sets the temporal fluctuation of the flow field at the last point N at the outlet equal to that of the second to last $N-1$. Additionally, a sponge region in the form of a source term $-\sigma \boldsymbol{q}'$ added to the right-hand side of (2.11) is used to force the perturbation field to a minimum in the outermost 2.5 % of the inlet and outlet regions to prevent reflection and numerical instability. This region is not regarded as part of the solution field. The distribution function

$$\sigma = \pm\sigma_{max}(1 - 6\hat{x}^5 + 15\hat{x}^4 - 10\hat{x}^3) \quad \text{on } \hat{x} \in [0, 1] \tag{2.15}$$

follows a fifth-order polynomial, where $\hat{x}$ is the locally scaled distance from the respective boundary. An amplitude $\sigma_{max} = 3$ was found sufficient for all cases. Harmonic perturbations are introduced into the domain by local heating strips. The perturbation introduction via the wall temperature is preferred over other means of triggering instabilities for mainly two reasons. First, temperature is a scalar field. Acting on the velocity field by wall blowing and suction leads to a problem in the corner region where any actuation always affects the low-speed near-wall region boundary layer on the opposite wall. Second, wall heating is most easily realisable in experiment in contrast to, for example, volume forcing. The enforced perturbation wall temperature follows, on both walls equally, a dipole distribution in the streamwise direction of the form

$$\left.\begin{aligned} T' &= \sum_{i=1}^{N} a_i \frac{81}{16}(2\hat{x})^3[3(2\hat{x})^2 - 7(2\hat{x}) + 4] \\ &\quad \times \cos(\omega_i t + \theta_{r,i}) \quad \text{on } \hat{x} \in [0, 0.5], \\ T' &= -\sum_{i=1}^{N} a_i \frac{81}{16}(2 - 2\hat{x})^3[3(2 - 2\hat{x})^2 - 7(2 - 2\hat{x}) + 4] \\ &\quad \times \cos(\omega_i t + \theta_{r,i}) \quad \text{on } \hat{x} \in [0.5, 1], \end{aligned}\right\} \tag{2.16}$$

to generate a superposition of N waves of individual amplitudes a_i, angular frequencies ω_i and random phases $\theta_{r,i}$. A dipole is preferred over a monopole distribution to keep the perturbation as energy-neutral as possible in an integral sense. Wherever active, the local heating strip replaces the adiabatic wall boundary condition (2.12). The perturbation strip is located between the streamwise locations $x_{p,0}$ and $x_{p,1}$ as given in table 2, corresponding to 30 grid cells, starting at the 15th grid point.

https://doi.org/10.1017/jfm.2014.31 Published online by Cambridge University Press

2.4. *Linear stability theory*

The stability of a steady base flow with respect to infinitesimally small disturbances is analysed in linear stability theory. Under the assumption that the base state $\boldsymbol{q}_0(\boldsymbol{x})$ is a solution to the Navier–Stokes equations and that terms that are quadratic in the disturbance are small and can be dropped, the evolution of a disturbance is governed by the linear perturbation equation

$$\frac{\partial \boldsymbol{q}'}{\partial t} = \mathscr{L}\boldsymbol{q}', \tag{2.17}$$

where $\mathscr{L}$ is the linearised operator. Equation (2.17) is cast into an eigenvalue problem by introducing a normal mode ansatz for $\boldsymbol{q}'$. Parallel flow is assumed for one- and two-dimensional base states. The ansatz reads $\boldsymbol{q}'(y,t) = \hat{\boldsymbol{q}}(y)\mathrm{e}^{\mathrm{i}(\alpha x+\beta z-\omega t)}$ for one-dimensional cases such as the classical flat-plate boundary layer, the asymptotic corner far-field solution or the flow along the corner bisector, and

$$\boldsymbol{q}'(y,z,t) = \hat{\boldsymbol{q}}(y,z)\mathrm{e}^{\mathrm{i}(\alpha x-\omega t)} \tag{2.18}$$

for a two-dimensional flow with just one homogeneous direction such as the self-similar corner flow solution we are primarily interested in. Here, wave-like behaviour of the perturbation is assumed by introducing a streamwise wavenumber α in the streamwise direction only. In any case, the amplitude function $\hat{\boldsymbol{q}}$ appears as the eigenvector and the angular frequency and wavenumber as eigenvalue or free parameter. If $\alpha \in \mathbb{R}$ and $\omega \in \mathbb{C}$, the perturbation amplitude A, e.g. $A \triangleq \|\hat{u}\|_\infty$, will change with time according to the relation $\mathrm{Im}(\omega) = (1/A)\,\partial A/\partial t$. This case is referred to as *temporal amplification theory*, and $\mathrm{Im}(\omega)$ represents the temporal amplification rate. In *spatial amplification theory*, $\omega \in \mathbb{R}$ is the free parameter, $\alpha \in \mathbb{C}$ appears as the eigenvalue and $-\mathrm{Im}(\alpha) = (1/A)\,\partial A/\partial x$ is identified as the spatial amplification rate. The temporal two-dimensional problem results in a $5N^2$ size eigenvalue problem

$$(\boldsymbol{L} + \boldsymbol{M}\omega)\hat{\boldsymbol{q}} = 0, \tag{2.19}$$

with $\hat{\boldsymbol{q}} = (\hat{\rho}, \hat{u}, \hat{v}, \hat{w}, \hat{T})^{\mathrm{T}}$, and the spatial problem in a $9N^2$ size eigenvalue problem

$$(\widetilde{\boldsymbol{L}} + \widetilde{\boldsymbol{M}}\alpha)\tilde{\boldsymbol{q}} = 0, \tag{2.20}$$

with $\tilde{\boldsymbol{q}} = (\hat{\rho}, \hat{u}, \hat{v}, \hat{w}, \hat{T}, \tilde{u}, \tilde{v}, \tilde{w}, \tilde{T})^{\mathrm{T}}$. As the eigenvalue α originally appears squared in the latter problem, it is rewritten as a first-order problem by use of the auxiliary variables $\tilde{u} = \alpha\hat{u}$, $\tilde{v} = \alpha\hat{v}$, $\tilde{w} = \alpha\hat{w}$ and $\tilde{T} = \alpha\hat{T}$. Here, $\boldsymbol{L}$, $\boldsymbol{M}$ and $\widetilde{\boldsymbol{L}}$, $\widetilde{\boldsymbol{M}}$ are the coefficient matrices of the discretised problems. Both problems are solved using the same spectral Chebyshev–Chebyshev collocation method on an $N = 45$ Gauss–Lobatto grid, and with the same validated parameters as for the temporal case in Schmidt & Rist (2011). Comprehensive introductions to one- and two-dimensional linear stability theory can be found in Mack (1984) and Theofilis (2003), respectively.

2.5. *Non-modal stability theory*

Linear stability theory governs the long-time response of infinitesimal perturbations. However, there are prominent examples of flows where short-term transient energy growth can lead to rapid transition, even when all eigenmodes decay exponentially. *A priori*, it is not clear whether a certain flow configuration is prone to transient growth.

https://doi.org/10.1017/jfm.2014.31 Published online by Cambridge University Press

In the corner flow case, the studies by Alizard *et al.* (2010, 2013) do suggest that this may well be the case. Transient amplification behaviour is directly linked to the non-normality of the linear operator. Therefore, it may be inappropriate to conclude anything about the stability of a flow just by examining individual eigenvalues if the linear operator is highly non-normal. Two aspects of non-modal stability theory are employed in § 5 to link the subcritical simulation results from § 4 to the linear stability results of § 3, namely ε pseudo-spectra to be introduced in the following § 2.5.1, and eigenvector expansion based optimal growth in § 2.5.2. The concept of normality necessitates a vector norm induced by an inner product $\langle . \rangle_E$ that we choose to be

$$\left.\begin{aligned} &\|\hat{\boldsymbol{q}}\|_E^2 = \langle \hat{\boldsymbol{q}}, \hat{\boldsymbol{q}} \rangle_E = \int_0^\infty \int_0^\infty \hat{\boldsymbol{q}}^H \boldsymbol{W} \hat{\boldsymbol{q}} \, \mathrm{d}y \, \mathrm{d}z, \\ &\text{where} \quad \boldsymbol{W} = \mathrm{diag}\{T/(\rho\gamma Ma^2),\, \rho,\, \rho,\, \rho,\, \rho/(\gamma(\gamma-1)TMa^2)\}, \end{aligned}\right\} \tag{2.21}$$

for $\hat{\boldsymbol{q}} = (\hat{\rho}, \hat{u}, \hat{v}, \hat{w}, \hat{T})^{\mathrm{T}}$ as the solution vector to (2.19) or (2.20) (Mack 1984), where superscript H denotes the conjugate transpose. The derivation of the above energy norm (2.21) for compressible gases can be found in Chu (1965) and Hanifi, Schmid & Henningson (1996). Here, we define the energy norm locally for the transverse plane spanned by y and z, i.e. as an energy density.

2.5.1. *ε-pseudospectrum*

The sensitivity of eigenvalues with respect to perturbations of the underlying linear operator can be determined by means of ε pseudo-spectra as shown by Trefethen (1991). The application to hydrodynamic problems was pioneered by Reddy, Schmid & Henningson (1993), and by Trefethen *et al.* (1993) shortly after. A complex number $\omega \in \mathbb{C}$ is in the ε pseudo-spectrum if

$$\|(\boldsymbol{M}\omega - \boldsymbol{L})^{-1}\|_E \geqslant \frac{1}{\varepsilon}, \tag{2.22}$$

where $(\boldsymbol{M}\omega - \boldsymbol{L})^{-1}$ is the resolvent and $\|.\|_E$ the energy norm defined in (2.21). Analogously, we define the resolvent for the spatial problem as

$$\|(\widetilde{\boldsymbol{M}}\alpha - \widetilde{\boldsymbol{L}})^{-1}\|_E \geqslant \frac{1}{\varepsilon}, \tag{2.23}$$

with $\alpha \in \mathbb{C}$. The isolines for a certain value of ε can intuitively be interpreted as the outer bound of all possible eigenvalues of the same operator, but randomly perturbed by superposition with a random perturbation matrix $\boldsymbol{P}$ of norm $\|\boldsymbol{P}\|_E \leqslant \varepsilon$. If ε is small, then a small perturbation of the linear system can lead to a response of substantial amplitude. Transient growth can be expected in the regions where the pseudo-spectrum extends the farthest into the unstable half-plane, and the corresponding frequencies/wavelengths can be determined. The case where a large response results from the non-normality of the underlying operator is referred to as *pseudo-resonance*, whereas the general term *resonance* refers to the situation where a system is forced close to one of its eigenvalues. Note that physical sensitivity due to non-normality and sensitivity with respect to discretisation errors of the numerical scheme cannot be distinguished without further examination (Schmid & Henningson 2001). The resolvent can be computed directly by means of singular value decomposition. However, we resort to the much more efficient routines of the EigTool library (Wright 2002).

https://doi.org/10.1017/jfm.2014.31 Published online by Cambridge University Press

2.5.2. *(Sub)optimal spatial perturbations*

Transient energy growth of an optimised initial condition was first calculated by Farrell (1988). The previously cited work of Reddy *et al.* (1993) ties directly into Farrell's work and connects to the concept of ε pseudo-spectra presented in § 2.5.1. As we are interested in the amplification behaviour downstream from a harmonic perturbation source, i.e. the signalling problem, we roughly follow Tumin & Reshotko (2001), who contributed decisively to the extension of the theory to spatial perturbations. The basic idea is to represent the downstream response $\boldsymbol{q}$ at some position x as the linear superposition

$$\boldsymbol{q}(\boldsymbol{x}, t) = \mathrm{e}^{-\mathrm{i}\omega t} \sum_{k=1}^{N} \kappa_k \hat{\boldsymbol{q}}_k(y, z) \mathrm{e}^{\mathrm{i}\alpha_k x} \tag{2.24}$$

of N eigenfunction solutions $\hat{\boldsymbol{q}}$ to the spatial stability problem (2.20). Here, it is assumed that the set of eigenvectors is a complete basis, i.e. that an arbitrary perturbation field can be constructed in terms of the sum in (2.24). If we restrict the expansion to some subspace $\mathbb{S}^N = \mathrm{span}\{\hat{\boldsymbol{q}}_1, \hat{\boldsymbol{q}}_2, \ldots, \hat{\boldsymbol{q}}_N\}$ of the full solution space, a suboptimal response is obtained. The expansion coefficients κ are calculated from the optimisation problem

$$G(x) = \max_{\boldsymbol{q}_0 \neq 0} \frac{\|\boldsymbol{q}(x)\|_E^2}{\|\boldsymbol{q}_0\|_E^2} \tag{2.25}$$

for the maximum energy growth $G(x)$ that relates the energy of the response $\|\boldsymbol{q}(x)\|_E^2$ to the energy of the initial condition $\|\boldsymbol{q}_0\|_E^2$ at the perturbation source location $x = 0$. For the practical solution of the optimisation problem (2.25), the energy norm is reduced to a standard L^2-matrix norm as $G(x) = \|\boldsymbol{F}\boldsymbol{\Lambda}_x\boldsymbol{F}^{-1}\|_2^2$, where $\boldsymbol{F}^H\boldsymbol{F} = \boldsymbol{C}$ is the Cholesky decomposition of the correlation matrix $\boldsymbol{C}$ with entries $C_{k,l} = \langle \hat{\boldsymbol{q}}_k, \hat{\boldsymbol{q}}_l \rangle_E$, and $\boldsymbol{\Lambda}_x = \mathrm{diag}\{\mathrm{e}^{\mathrm{i}\alpha_1 x}, \mathrm{e}^{\mathrm{i}\alpha_2 x}, \ldots, \mathrm{e}^{\mathrm{i}\alpha_N x}\}$. Now, $G(x)$ can readily be obtained as the L^2-matrix norm of $\boldsymbol{F}\boldsymbol{\Lambda}_x\boldsymbol{F}^{-1}$ in the form of its principal singular value σ_1. The reader is referred to Schmid & Henningson (1994) for further details.

The latter method of representing local optimal solutions in terms of a linear combination of eigenfunctions is preferred for our work as it allow us to directly relate linear stability results to non-modal growth. By looking at the factors in the expansion equation (2.24), it becomes clear that transient growth of the norm of the sum can occur if the eigenvectors are non-orthogonal, even if $\mathrm{Im}(\alpha) \geqslant 0$ for all α. The expansion coefficients κ are used to reconstruct the optimal solution from (2.24), and give valuable information on the modes involved in the transient growth process.

2.6. *Dynamic mode decomposition*

The dynamic mode decomposition extracts coherent structures as well as their corresponding frequencies and growth rates from a time series of snapshots of a flow field. The method is based on the spectral analysis of the Koopman operator, which maps an observable of a dynamical system to its next instant. In the context of DNS, the whole flow field can be taken as the observable and the resulting modes resemble global modes of a single frequency. Classical global linear stability modes are obtained from linearised flow dynamics or flow fields that are generated by a nonlinear code but with small perturbations. However, the decomposition is not restricted to the linear regime. It is equally valid for fully nonlinear flows where the modes accurately capture the dynamical behaviour as demonstrated by Rowley *et al.*

https://doi.org/10.1017/jfm.2014.31 Published online by Cambridge University Press

(2009) and Bagheri (2013) for the case of a jet in cross-flow and a cylinder wake, respectively. The reader is referred to the latter citations for a detailed introduction to Koopman-operator-based spectral analysis. In the DNS context, the terms 'Koopman mode' and 'dynamic mode' are equivalent. The dynamic mode decomposition (DMD) was introduced by Schmid (2010) as a robust and efficient method of computation. In linear stability theory, the long-time behaviour of a given base flow is examined by an eigenvalue decomposition of the governing linear stability operator as described in § 2.4. Similar information can be extracted from a time series of N consecutive snapshots in the form of a matrix,

$$\boldsymbol{Q}_1^N = [\boldsymbol{q}'_1 \quad \boldsymbol{q}'_2 \quad \boldsymbol{q}'_3 \quad \dots \quad \boldsymbol{q}'_N] \tag{2.26a}$$

$$= [\boldsymbol{q}'_1 \quad \boldsymbol{A}\boldsymbol{q}'_1 \quad \boldsymbol{A}^2\boldsymbol{q}'_1 \quad \dots \quad \boldsymbol{A}^{N-1}\boldsymbol{q}'_1], \tag{2.26b}$$

under the assumption of a linear mapping $\boldsymbol{A}$ that carries a snapshot to the next time instant, that is,

$$\boldsymbol{q}'_{i+1} = \boldsymbol{A}\boldsymbol{q}'_i. \tag{2.27}$$

The notional time series (2.26*a*)(*b*) is referred to as a Krylov sequence. The linear mapping or propagator $\boldsymbol{A}$ is closely related to the linear stability operator $\mathscr{L}$ defined in (2.17) and its eigenvalues can be approximated by the eigenvalues of a matrix $\tilde{\boldsymbol{S}} = \boldsymbol{U}^H \boldsymbol{Q}_2^N \boldsymbol{W} \boldsymbol{\Sigma}^{-1}$, where the factors on the right-hand side originate from a singular value decomposition $\boldsymbol{Q}_1^N = \boldsymbol{U}\boldsymbol{\Sigma}\boldsymbol{W}^H$ of the snapshot matrix (2.26*a*) and $\boldsymbol{Q}_2^N = [\boldsymbol{q}'_2\, \boldsymbol{q}'_3\, \boldsymbol{q}'_4 \dots \boldsymbol{q}'_N]$. The eigenvalues λ_i of $\tilde{\boldsymbol{S}}$ are then a subset of the eigenvalues of $\boldsymbol{A}$ defined through the equality $\tilde{\boldsymbol{S}}\boldsymbol{y}_i = \lambda_i \boldsymbol{y}_i$, with $\boldsymbol{y}_i$ being the corresponding eigenvectors. The ith dynamic mode $\boldsymbol{\phi}_i$ is obtained as

$$\boldsymbol{\phi}_i = \boldsymbol{U}\boldsymbol{y}_i, \tag{2.28}$$

and the complex frequency is recovered as $\omega_i = \log(\lambda_i)/\Delta t$ with Δt as the time interval between two snapshots. As the Koopman modes are interpreted as global stability modes in our case, we choose the same notation for the solution vector, i.e. $\boldsymbol{\phi} = (\hat{\rho},\, \hat{u},\, \hat{v},\, \hat{w},\, \hat{T})^{\mathrm{T}}$. We prefer the DMD over a traditional temporal discrete Fourier transform (DFT) for the reasons elaborated by Chen, Tu & Rowley (2011). First, by subtracting an *equilibrium point* of the dynamics, i.e. the laminar base state $\boldsymbol{q}_0$ from § 2.2, the calculated DMD modes will satisfy homogeneous boundary conditions and be solutions to the linearised dynamics (2.17). In general, the zeroth Fourier component, i.e. the mean field, is not a solution to the steady dynamics, and the higher Fourier modes are not solutions to the linearised transient dynamics. The second argument is that DMD recovers growth rates. However, this argument does not directly apply to our case since the problem is convective. All modal growth rates are expected to vanish for that reason, corresponding to all λ_i lying on the unit disc in the complex plane.

3. Spatial linear stability analysis

The spatial linear stability problem was previously considered by Galionis & Hall (2005) for incompressible corner flow. By space marching the parabolised stability equations (PSE), the authors calculated the amplification behaviour of selected modes. We are, however, interested in connected branches of discrete modes, and choose to solve the spatial eigenvalue problem (2.20) instead. The structure of the spatial spectrum is found to be comparable to the temporal spectrum as shown in figure 3. For now, we restrict our attention to the relevant part of the spectrum containing

https://doi.org/10.1017/jfm.2014.31 Published online by Cambridge University Press

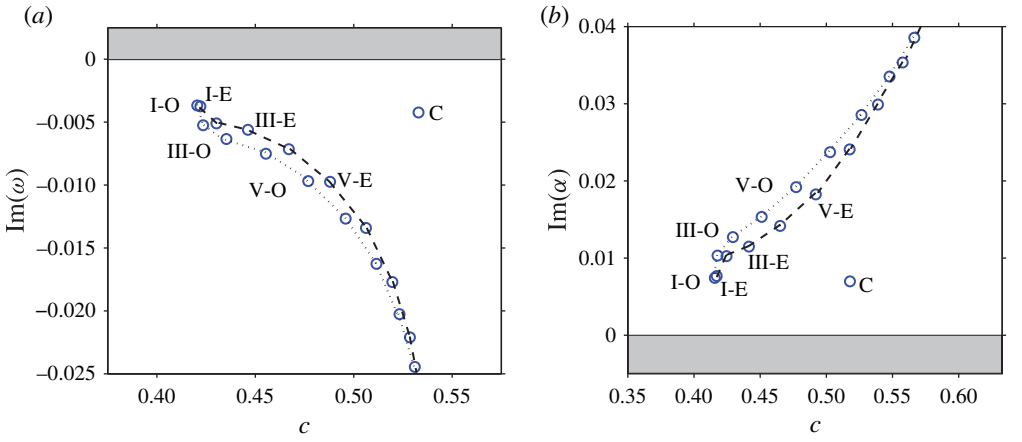


FIGURE 3. Comparison between temporal and spatial discrete branch solutions at $Re_x = 57\,500$: (*a*) temporal spectrum for $\alpha = 0.1412$; (*b*) spatial spectrum for $\omega = 0.1$. The grey shaded areas represent the respective unstable half-planes. Dashed lines connect the even symmetric (E) modes, and dotted lines connect odd symmetric (O) modes. The inviscid corner mode is marked as C. The free parameters are chosen in such a way that the fundamental symmetric TS mode (I-E) has the same phase speed in both cases.

the Tollmien–Schlichting (TS) like eigenmode branch and the isolated inviscid corner mode. Viscous modes are found to be either even (E) or odd (O) symmetric with respect to the corner bisector, and are sorted in increasing order by the number of maxima of the perturbation amplitude along the spanwise directions, or equivalently by the spanwise wavenumber (capital Roman numerals). The fundamental modes I-E and I-O have only one maximum along each spanwise coordinate located on the far-field boundaries, while modes downwards (upwards) from the branches of the temporal (spatial) solution possess higher spanwise wavenumbers dictated by the computational domain extent.

Examples of the three categories of relevant spatial modes are depicted in figure 4. Note that even symmetric modes feature a local amplitude maximum whereas odd symmetric modes are null along the corner bisector, and that the inviscid mode shown in figure 4(*c*) is symmetric, and has no significant spatial support for $(\eta, \zeta) \gtrsim 15$. It was shown by Schmidt & Rist (2011) that the corner mode has an odd symmetric counterpart that becomes relevant at supersonic speeds but does not appear in the $Ma = 0.8$ case at hand.

The neutral stability diagram shown in figure 5 is constructed from a 15×45 solution grid in the parameter space $(\omega, Re_x) \in [0.03, 0.15] \times [8.5 \times 10^4, 5 \times 10^5]$. At each point, 25 modes of the discrete branch (including the corner mode) are calculated using the shift-and-invert Arnoldi method. Neutral stability curves of individual modes are found in a post-processing step by cross-correlation. A critical Reynolds number of $Re^{\mathrm{I-O}}_{x,crit} \approx 1.32 \times 10^5$ is found, occurring for mode I-O at $\alpha^{\mathrm{I-O}}_{crit} \approx 0.11$. The corner mode becomes first unstable at $Re^{\mathrm{C}}_{x,crit} \approx 2.54 \times 10^5$, and for $\alpha^{\mathrm{C}}_{crit} \approx 0.084$. It can be seen that the stability characteristics of even and odd symmetric perturbations are similar. The two-dimensional corner flow results shown compare well with the literature in the sense that the linear stability results are similar to one-dimensional (Blasius) flat-plate solutions but with a somewhat higher critical Reynolds number, and no significant difference between spatial and temporal theory is observed. The latter statement was

https://doi.org/10.1017/jfm.2014.31 Published online by Cambridge University Press

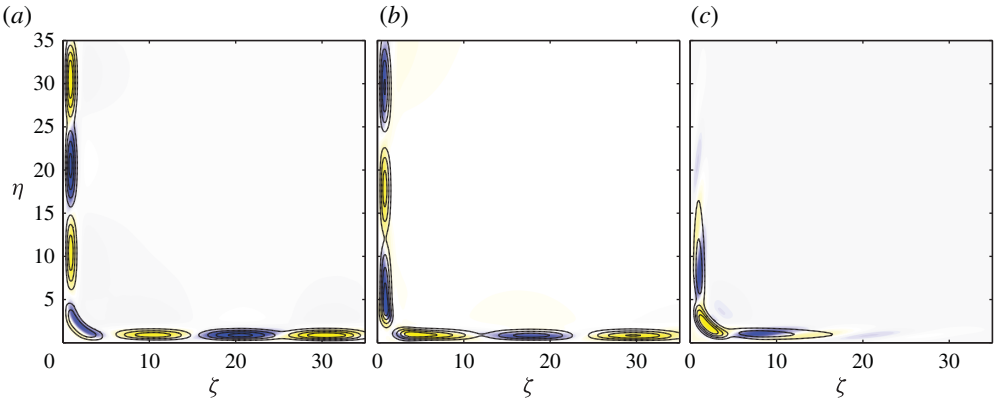


FIGURE 4. Three examples of spatial eigenfunctions of the streamwise perturbation velocity $\hat{u}$ for $Re_x = 57\,500$, $\omega = 0.12$: (*a*) symmetric mode IV-E; (*b*) odd symmetric mode IV-O; (*c*) corner mode. Solid lines represent constant values of $\|\hat{u}\|$, blue isocontours are values of $\mathrm{Re}(\hat{u}) > 0$, and yellow isocontours are values of $\mathrm{Re}(\hat{u}) < 0$.

confirmed by mutually converting the results using Gaster's transformation (Gaster 1962), i.e. $\mathrm{Im}(\alpha) \approx -\mathrm{Im}(\omega)/c$.

4. Direct numerical simulation

For comparison with linear theory, we are interested in a broad-band response of the base flow to harmonic forcing. A total of 30 harmonic perturbations in the form of a uniformly spaced frequency band $\omega_i \in [0.01, 0.3]$, and of random phase are forced in the DNS set-up summarised in table 2 by means of wall heating (2.16). The Reynolds-number regime under investigation is subcritical in terms of linear stability theory, see figure 5. Therefore, all perturbations are expected to decay monotonically. Wall-bounded instabilities, such as Tollmien–Schlichting waves, are usually found to behave linearly for perturbation amplitudes $< 1\,\%$ of the free-stream velocity. Here, we use the term *linear* if the amplification rate is independent of the actual perturbation amplitude, and hence in agreement with the linear ansatz. A maximum streamwise perturbation amplitude of $\|u'\|_\infty \lesssim 5 \times 10^{-6}$ was realised to guarantee linear behaviour within the subdomain used for the spectral analysis by setting the temperature amplitude coefficient to $a_i = 1 \times 10^{-5}$.

4.1. *Spectral analysis*

The dynamic mode decomposition method described in § 2.6 enables us to extract discrete frequency components in the form of global coherent structures from DNS data. The initial transients before the perturbations reach the outlet of the computational box are ignored, i.e. only time-periodic data are analysed. The receptivity process that translates the initial temperature forcing to the final convective instability is spatially localised in the direct vicinity of the heating strip, and is also excluded from the analysis by conducting the decompositions within a subdomain that starts at a distance $x = 110$ somewhat downstream of the wall heating. A Krylov sequence of 125 snapshots, $\boldsymbol{Q}_1^{125}$, over one fundamental period determined by the lowest frequency component $\omega_{min} = 0.01$ is used for the DMD.

https://doi.org/10.1017/jfm.2014.31 Published online by Cambridge University Press

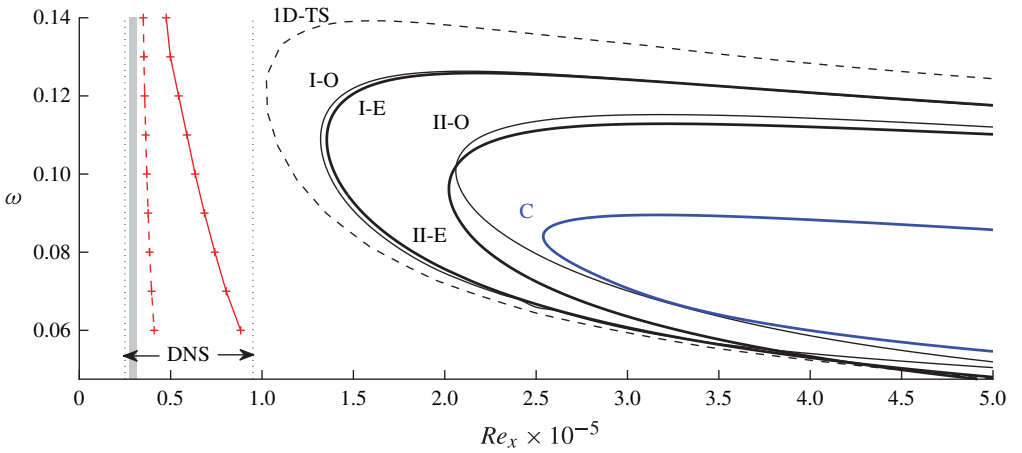


FIGURE 5. Spatial neutral stability diagram. The neutral stability curve (dashed) of the one-dimensional asymptotic far-field solution $(\rho_0, u_0, v_1, w_1, T_0)^{\mathrm{T}}$ is shown for comparison. The computational domain extent of the DNS (dotted vertical lines) and the perturbation strip location (shaded grey band) are depicted for later reference in § 4, as well as the first (red dashed line with + signs) and second (red full line with + signs) neutral points of the global (DMD) modes.

The Ritz circle and the modal amplitudes of the decomposition are depicted in figure 6. It can be seen from figure 6(*a*) that the empirical Ritz values corresponding to the forced frequencies, and their conjugate complex counterparts lie on the unit disc. This agrees with the expectation of zero temporal amplification in the case of a statically stationary process. The remaining modes are identified as nonlinearly generated higher harmonics, and numerical artefacts of very low amplitude. A reconstruction of instantaneous flow fields from the reduced set of modes corresponding to the 30 forcing frequencies recovers $> 99.5\,\%$ of the global perturbation energy. It is hence concluded that the decomposition is well converged, and that nonlinear effects are negligible.

Examples of three global modes are visualised in figure 7. All three modes exhibit two distinct features: a parallel modulated wave train along both walls that is readily identified as Tollmien–Schlichting instability, and a perturbation pattern consisting of Λ-shaped structures in the near-corner region. Note that the two features appear increasingly separated from each other with increasing downstream distance, suggesting the possibility of different spatial amplification behaviour. The two structures can be examined individually and in more detail in the planar contour plots of the modal streamwise perturbation velocity presented in figure 8. Here, the $\omega = 0.13$ mode is chosen as a representative example. The far-field plane in figure 8(*a*) shows the characteristic signature of a Tollmien–Schlichting wave. It can be seen that the perturbation decays monotonically while being convected in the streamwise direction. The decay rate is in agreement with the linear stability results for the one-dimensional far-field profile previously presented in figure 5. An inspection of perturbation isolines in the bisector plane shown in figure 8(*b*) reveals major differences from the Tollmien–Schlichting wave. The perturbation pattern appears tilted in the direction of the mean shear, and its maxima are located at a higher distance from the wall. Most notably, the perturbation appears to grow spatially

https://doi.org/10.1017/jfm.2014.31 Published online by Cambridge University Press

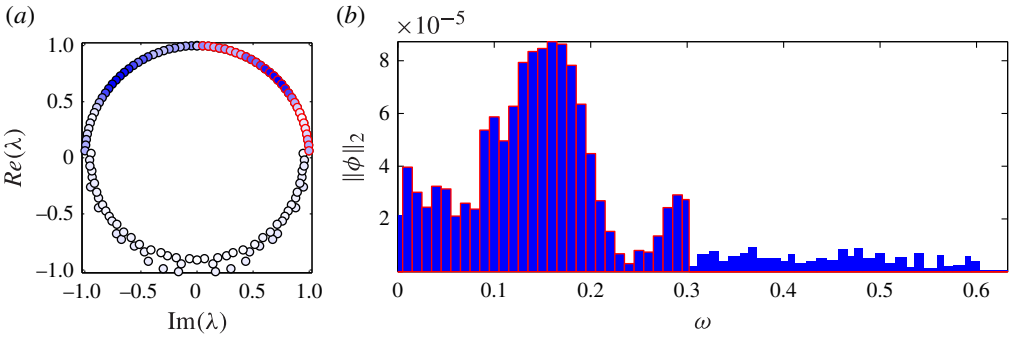


FIGURE 6. Dynamic mode decomposition of the DNS data: (*a*) empirical Ritz values λ_i; (*b*) magnitude of the Koopman modes. The colours in panel (*a*) vary smoothly from blue to white, depending on the modal amplitude. Modes corresponding to the forcing frequencies are highlighted by red circles in (*a*) and by red outlined bars in (*b*).

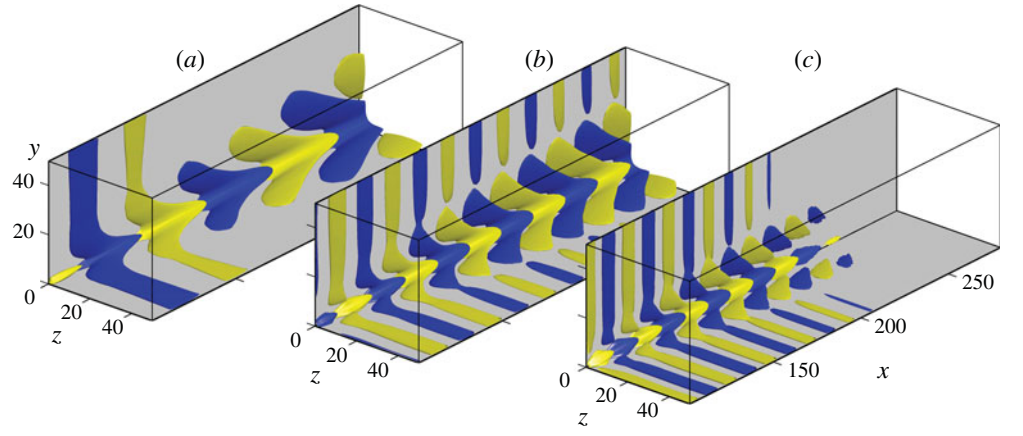


FIGURE 7. Examples of dynamic modes visualised by isosurfaces of the streamwise perturbation velocity: (*a*) $\omega = 0.04$, (*b*) $\omega = 0.09$, (*c*) $\omega = 0.13$. Isosurfaces are drawn at $\hat{u}/\|\hat{u}\|_\infty = 0.2$ (yellow) and $\hat{u}/\|\hat{u}\|_\infty = -0.2$ (blue).

over some distance. This behaviour is in contradiction to the linear stability results. However, the latter statement stems from qualitative observations of the flow field. In the next step (§ 4.2), we seek quantitative confirmation by considering an integral measure of perturbation energy that allows direct comparison with linear theory.

4.2. *Spatial amplification behaviour*

The modal spatial amplification behaviour is to be expressed in terms of the compressible energy norm (2.21). For the case at hand, it has to be taken into account that the base flow is non-parallel, the perturbation field has no compact support, and the amplification behaviour differs regionally as observed in § 4.1. The effect of non-parallelism, i.e. boundary-layer growth, can be eliminated by applying the self-similar transformation (2.6) to the spanwise coordinates with a fixed upper integration limit. The amplification behaviour of the Λ structure is isolated from the decaying Tollmien–Schlichting wave train by choosing an appropriate upper limit. As

https://doi.org/10.1017/jfm.2014.31 Published online by Cambridge University Press

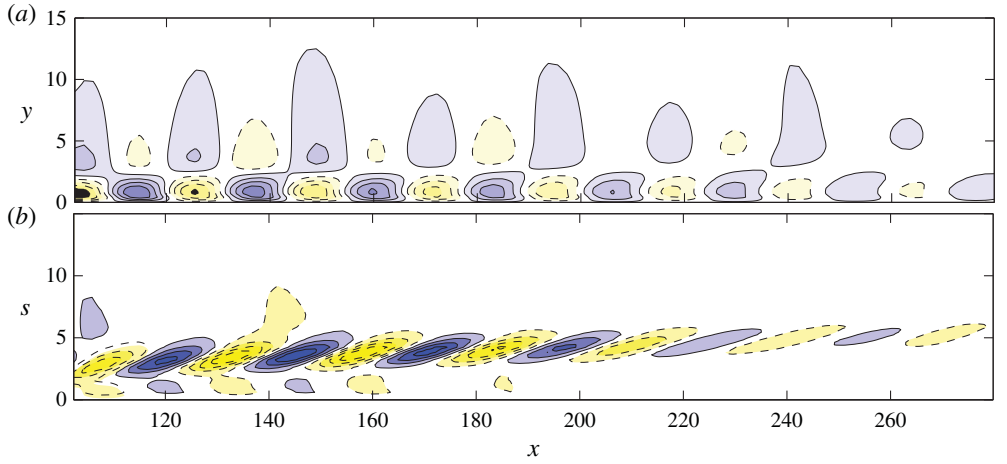


FIGURE 8. Planar views of the streamwise perturbation velocity of the Koopman mode corresponding to $\omega = 0.13$: (*a*) far-field plane (x, y) at $z = 50$; (*b*) corner bisector plane (x, s), where $y = z$. Isolines are drawn at equally spaced values of $\hat{u}/\|\hat{u}\|_\infty > 0$ (blue, full line) and $\hat{u}/\|\hat{u}\|_\infty < 0$ (yellow, dashed line).

it happens, the amplification behaviour was found to be rather insensitive to the exact choice of the upper integration limit. Almost identical curves are obtained within a regime of 10 ± 2. Hence, we define

$$\|\boldsymbol{\phi}\|_C^2 = \langle \boldsymbol{\phi}, \boldsymbol{\phi} \rangle_C = \int_0^{10} \int_0^{10} \boldsymbol{\phi}^H \boldsymbol{W} \boldsymbol{\phi} \, \mathrm{d}\eta \, \mathrm{d}\zeta \tag{4.1}$$

as an appropriate quantity to quantify the near-corner perturbation evolution. For mutual comparison, and comparison with linear theory, the modal amplification curves are normalised with respect to the energy $\|\boldsymbol{\phi}\|_{c,0}$ at the respective first neutral point, yielding the normalised energy density

$$d_E = \frac{\|\boldsymbol{\phi}\|_c}{\|\boldsymbol{\phi}\|_{c,0}}. \tag{4.2}$$

The streamwise location of $\|\boldsymbol{\phi}\|_{c,0}$ is found for each mode at the transition point between the energy decay downstream of the receptivity region, and the onset of spatial amplification, i.e. at the position where $\partial \|\boldsymbol{\phi}\|_c / \partial x = 0$. This procedure is successfully applied for all global modes with $\omega < 0.19$. No spatial amplification is observed below that value. Figure 9(*a*) depicts the modal amplification curves, and figure 9(*b*) the derivative of the latter in the streamwise direction. Only modes that possess a second extremum in the form of a maximum, i.e. all modes with $\omega > 0.06$, are depicted. After a short initial transient that is qualitatively similar for all curves, it can be seen that lower-frequency curves undergo a change of slope while a simpler shape is observed for higher ω. This behaviour becomes more apparent when considering the slope directly, as in figure 9(*b*). Modes with $\omega \gtrsim 0.11$ possess a parabola-like slope distribution, while a second extremum emerges for small frequencies, resulting in a second inflexion point for $\omega \leqslant 0.8$.

The first and second neutral points of each frequency are also incorporated into figure 5 (dashed and solid red line, respectively). The fact that the observed spatial

https://doi.org/10.1017/jfm.2014.31 Published online by Cambridge University Press

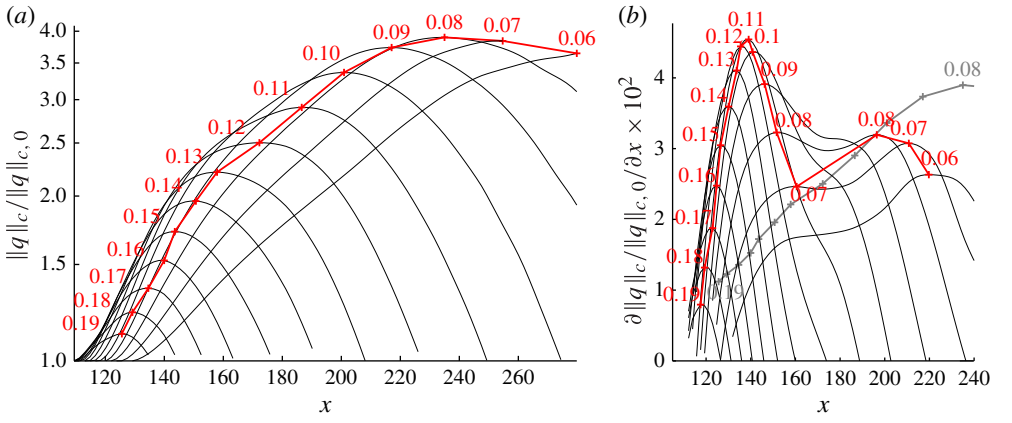


FIGURE 9. Modal perturbation amplification in the corner region: (*a*) downstream development of the perturbation energy density d_E for different modes; (*b*) downstream rate of change of d_E. The line connecting the modal maxima is shown (red line with + signs) along with the corresponding modal frequencies (red numbers). The line of maxima from panel (*a*) is reproduced in (*b*) for comparison (grey line with + signs).

growth between the resulting neutral curves occurs in a region that is predicted to be stable by linear theory suggests that physical mechanisms different from exponential growth of normal-form perturbations are at play.

4.3. *Energetic analysis*

More insight into the nature of a perturbation can be gained by considering the modal energy balance, i.e. by analysing certain terms of the perturbation kinetic energy transport equation

$$\rho\frac{\mathrm{D}k}{\mathrm{D}t} = \underbrace{\mathscr{D}_t}_{\text{turbulent diffusion}} + \underbrace{\mathscr{D}_v}_{\text{viscous diffusion}} + \underbrace{\mathscr{P}}_{\text{production}} + \underbrace{\varepsilon_k}_{\text{dissipation}} . \tag{4.3}$$

Here, $k=\frac{1}{2}(\overline{u'^2+v'^2+w'^2})$ is the perturbation kinetic energy, and $\mathrm{D}/\mathrm{D}t=\partial/\partial t+\boldsymbol{u}\cdot\boldsymbol{\nabla}$ the material derivative. In particular, the production term

$$\begin{aligned}\mathscr{P} = -\rho\Bigg(&\overline{u'^2}\frac{\partial u}{\partial x}+\overline{u'v'}\frac{\partial v}{\partial x}+\overline{u'w'}\frac{\partial w}{\partial x}\overline{u'v'}\frac{\partial u}{\partial y}\\ &+\overline{v'^2}\frac{\partial v}{\partial y}+\overline{v'w'}\frac{\partial w}{\partial y}\overline{u'w'}\frac{\partial u}{\partial z}+\overline{v'w'}\frac{\partial v}{\partial z}+\overline{w'^2}\frac{\partial w}{\partial z}\Bigg)\end{aligned} \tag{4.4}$$

is of interest. By calculating each term individually, it is found that the two terms associated with the work of the Reynolds stress tensor against the transverse shear components, $\partial u/\partial y$ and $\partial u/\partial z$, are dominant, as typically observed for wall-bounded shear-flow instabilities. The two terms are combined into a single quantity $\mathscr{P}_u=\overline{u'v'}\,\partial u/\partial y+\overline{u'w'}\,\partial u/\partial z$. The perturbation energy production in terms of $\mathscr{P}_u$ is visualised in figure 10. For comparison, the same mode as depicted in figure 8 is analysed. On the bisector plane in figure 8(*a*), the energy production

https://doi.org/10.1017/jfm.2014.31 Published online by Cambridge University Press

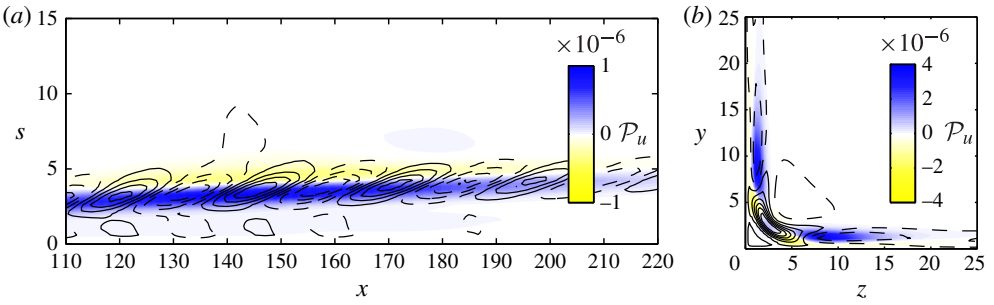


FIGURE 10. Planar views of the perturbation kinetic energy production $\mathscr{P}_u$ of the Koopman mode corresponding to $\omega = 0.13$: (*a*) corner bisector plane (x, s), where $y = z$; (*b*) transverse plane (y, z) at $x = 145$. Isolines are drawn at equally spaced values of $\hat{u}/\|\hat{u}\|_\infty > 0$ (full line) and $\hat{u}/\|\hat{u}\|_\infty < 0$ (dashed line).

is shown to coincide closely with the perturbation field. When comparing with the representative transverse plane cut shown in figure 8(*b*), it can be seen that the production of k is exclusively restricted to the near-corner region, and that the overall maximum is located along the outer parts of the Λ structure. The observation that $\mathscr{P}_u$ is not evenly distributed in coincidence with the perturbation field itself, and is partly negative, suggests an ongoing deformation of the structure in both planes. The examination of one-dimensional flow-field profiles extracted from the transverse plane permits an even closer look at the instability mechanism. Profiles along and parallel to the bisector at four different spanwise locations are plotted in figure 11(*a–d*). The streamwise base-flow profile can be compared directly with the perturbation energy production distribution and the streamwise perturbation amplitude. Also, the profiles can be related to the wall-normal position of the critical layer, and the inflexion point in the base flow. Along the bisector coordinate, as shown in figure 11(*a*), the maximum of the perturbation amplitude and the maximum of perturbation energy production approximately coincide with the location of the critical layer and the inflexion point. Therefore, the Rayleigh–Fjørtoft necessary criterion for inviscid instability is met (see e.g. Drazin & Reid 2004). In figure 11(*b*), the ordinate is positioned such that the profiles represent the region of maximum perturbation energy production, i.e. within the outer part of the Λ structure (compare figure 8*b*). Here, we note that the maxima of the perturbation amplitude and production also coincide with the critical layer but not, however, with the location of the inflexion point. The perturbation's footprint resembles that of a viscid instability, as the necessary criterion for inviscid instability is hence not met in this case. The transition to a Tollmien–Schlichting type of instability towards the far field is portrayed in figure 11(*c,d*). It can be seen that the perturbation energy production is dominantly negative, in accordance with the predicted monotonic decay of the one-dimensional Tollmien–Schlichting wave.

4.4. *Note on bisector symmetry*

In a second DNS of the same set-up, a $\Delta\theta = \pi$ phase shift between the perturbations along the two walls was enforced in (2.16) to consider the behaviour of odd symmetric perturbations. However, no spatial amplification was detected within the computational domain, unlike in the symmetric case discussed so far. This is another

https://doi.org/10.1017/jfm.2014.31 Published online by Cambridge University Press

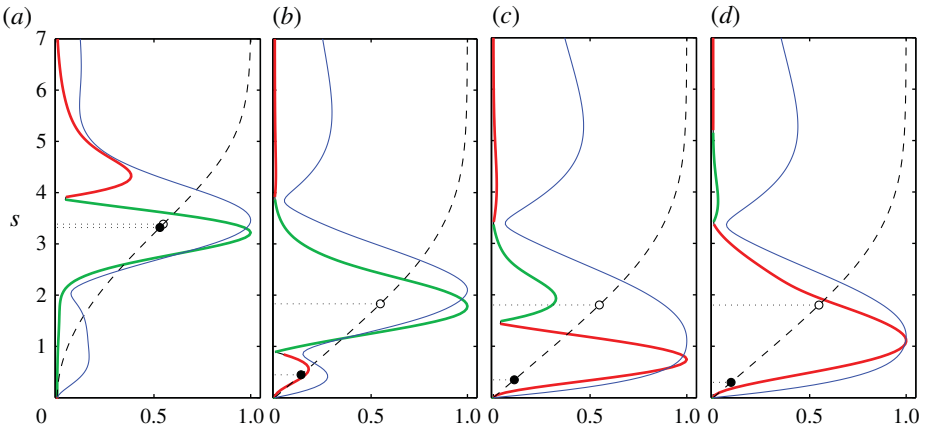


FIGURE 11. Profiles of the streamwise base-flow component u (dashed line), streamwise perturbation amplitude $\|\hat{u}\|/\|\hat{u}\|_\infty$ (blue full line), and kinetic energy production amplitude $\|\mathscr{P}_u\|/\|\mathscr{P}_u\|_\infty$ with $\mathscr{P}_u > 0$ (green full line) and $\mathscr{P}_u < 0$ (red full line), respectively. Profiles are drawn for $x = 145$ along 45° angle lines to the lower wall parallel to s starting at: (*a*) $(y_0, z_0) = (0, 0)$, i.e. along s; (*b*) $(y_0, z_0) = (0, 7.25)$; (*c*) $(y_0, z_0) = (0, 20)$; and (*d*) $(y_0, z_0) = (0, 30)$. Additionally, the position of the inflexion point (filled circle) and the critical layer (open circle) are indicated. The critical layer is determined for a group velocity of $c_g = 0.548$, estimated from the local modal perturbation wavelength.

indication for the prominent role of the inviscid corner mode, as no such mode is present in the asymmetric case for the parameter regime under consideration.

5. Local non-modal analysis

Whenever linear stability theory fails to predict perturbation amplification even though all underlying assumptions, i.e. local parallelism and linearity, are met, it is strongly suggested that non-modal (transient) behaviour is observed (Trefethen *et al.* 1993).

5.1. *Resolvent-based sensitivity*

In the following, the non-normality of the temporal and spatial discretised linear stability operator is addressed by means of the resolvent norm introduced in § 2.5.1. Figure 12 compares the temporal and spatial ε pseudo-spectra. It can be seen that the magnitude and the distribution of the resolvent norm are similar. In both cases, the values of ε are several orders of magnitudes lower than for a normal operator, suggesting a strong non-normality. The imprint of the Tollmien–Schlichting branch on the isolines is obvious, while almost no deformation is observed in the vicinity of the corner mode. This can be explained by the fact that the spatial support of the corner mode differs from that of the viscous modes (see figure 4).

The distribution of the resolvent norm along the real axis is an indicator of where to expect non-modal interactions in parameter space, i.e. in the region where the resolvent attains its minimum value. The free parameters (α, Re_x) in the temporal case and (ω, Re_x) in the spatial case are varied with the other parameter fixed in figure 13(*a*,*b*) and figure 13(*c*,*d*), respectively. In the temporal case, the lowest values of the resolvent are found for low values of α (figure 13*a*) and high values of Re_x

https://doi.org/10.1017/jfm.2014.31 Published online by Cambridge University Press

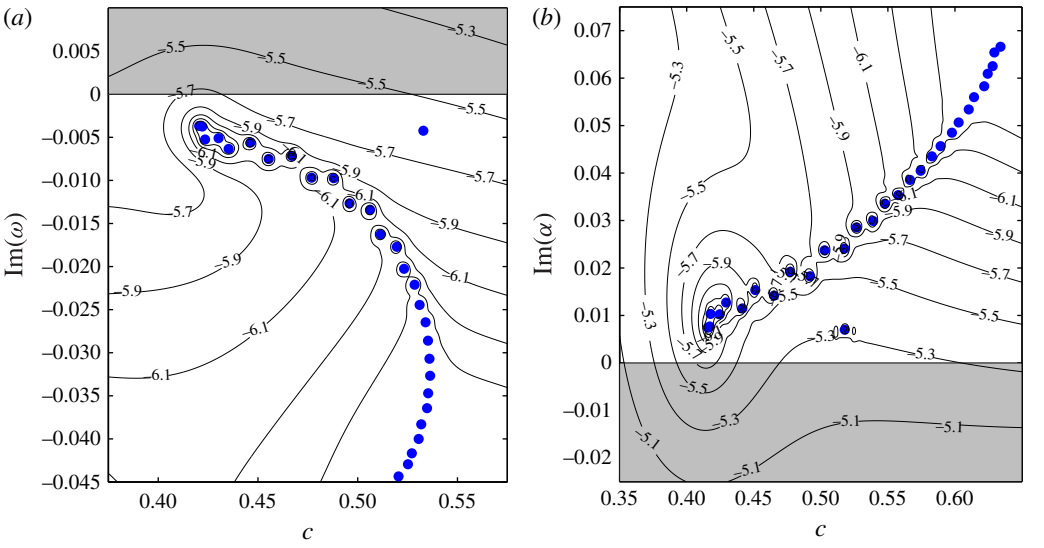


FIGURE 12. Isolines of the resolvent norm on a $\log_{10}$ scale (full lines) and eigenvalues (blue circles) for the same parameters as in figure 3: (*a*) temporal and (*b*) spatial ε pseudo-spectra. The grey shaded areas mark the unstable region.

(figure 13*b*). The latter observation is highly expected as the entire discrete spectrum moves towards the unstable half-plane with increasing Re_x due to the convectively unstable nature of the problem. The same Reynolds number dependence holds in the spatial case (see figure 13*d*). In any of the above cases, the position of the minimum resolvent associates the non-normality predominantly with the viscous branch at typical phase velocities of $0.3 \lesssim c \lesssim 0.45$. Low values of α for the maximum in the temporal case agree with the common notion that non-modal behaviour, i.e. pseudo-resonance, is associated with long wavelengths. A qualitatively different behaviour is observed for the dependence of the resolvent on the frequency as shown in figure 13(*c*), where the minimum resolvent abruptly jumps towards higher phase velocities when the frequency is decreased below $\omega \approx 0.05$, and a local minimum is identified at $(\omega, c) \approx (0.11, 0.43)$. Hence, pseudo-resonance is expected simultaneously within two different spanwise wavenumber regimes for low frequencies. Remarkably, the frequency of the local minimum coincides with the frequency associated with the maximum streamwise rate of change of the perturbation energy when compared to the DNS results in figure 9(*b*). The possible distinction of two different mechanisms deduced from the simulation data is supported by the present nonlinear analysis. However, only the spatial non-modal approach predicts a non-monotonic dependence on frequency, even though spatial and temporal linear stability calculations are found to be equivalent when converted into each other by means of Gaster's transformation.

5.2. *Suboptimal transient growth*

In the following, suboptimal non-modal spatial amplification is predicted by means of the linear stability eigenfunction expansion technique introduced in § 2.5.2. Here, we refer to *suboptimal* transient growth because the optimal gain is sought within a limited subspace of the full solution space of the linear operator. If not mentioned

https://doi.org/10.1017/jfm.2014.31 Published online by Cambridge University Press

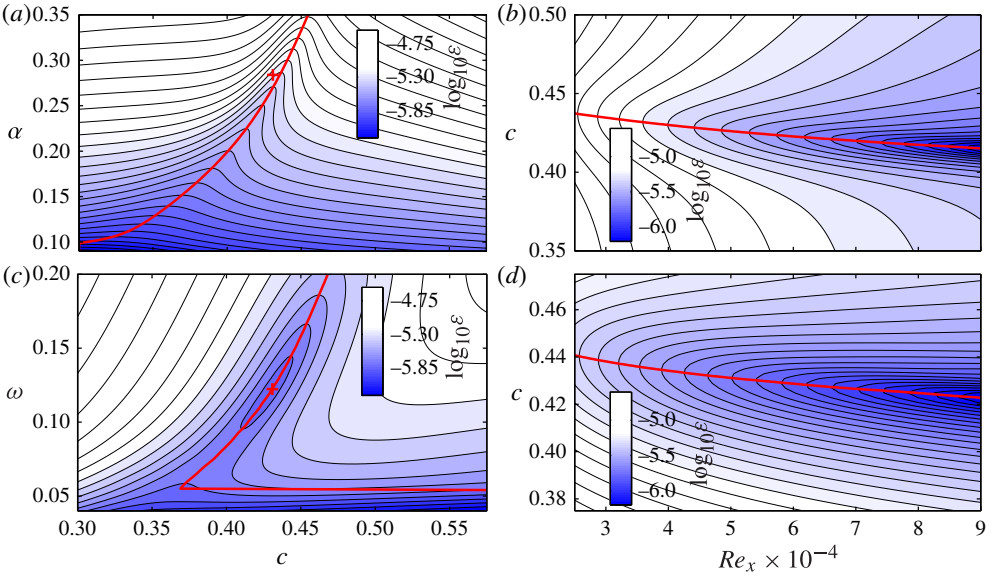


FIGURE 13. Values of the resolvent norm along the real axis: (*a*) as a function of α at a fixed $Re_x = 57\,500$; (*b*) as a function of Re_x at a fixed $\alpha = 0.25$; (*c*) as a function of ω at a fixed $Re_x = 57\,500$; and (*d*) as a function of Re_x at a fixed $\omega = 0.12$. (*a*,*b*) The temporal and (*c*,*d*) the spatial cases. The lines of maximum resolvent norm as a function of the free parameter (red full line) and a local maximum (red + sign) found for the spatial case in panel (*c*) are indicated separately. The latter local maximum is transferred to panel (*a*) using the local group velocity $c_g = 0.43$.

otherwise, the subspace

$$\mathbb{S}^{\mathrm{TS}\cup\mathrm{C}} = \mathrm{span}\{\hat{\boldsymbol{q}}^{\mathrm{C}}, \hat{\boldsymbol{q}}^{\mathrm{I-E}}, \hat{\boldsymbol{q}}^{\mathrm{I-O}}, \hat{\boldsymbol{q}}^{\mathrm{II-E}}, \hat{\boldsymbol{q}}^{\mathrm{II-O}}, \ldots\}, \tag{5.1}$$

consisting of the 29 leading (even or odd symmetric) Tollmien–Schlichting modes and the corner mode, is used. The underlying assumption is that the wall-bounded perturbation waves introduced in the direct simulation can be represented by the latter wall-bounded set of eigenmodes, and has to be confirmed *a posteriori*. For now, the assumption is solely based on the simple geometric argument of comparable spatial support. The local analysis is conducted for $Re_x = 57\,500$, which corresponds to the middle of the computational domain, and is a somewhat arbitrary (least-biased) choice. The spectral distribution of the modal expansion coefficients and the associated optimal initial condition for $\omega = 0.13$ are depicted in figure 14(*a*,*b*), respectively. From figure 14(*a*), it can be seen that only even symmetric modes contribute to the expansion. The highest expansion coefficient is found for mode II-E, corresponding to $\approx 25\,\%$ of the total sum, while a moderate contribution of $\approx 8\,\%$ is found for the corner mode. The spatial structure of the resulting suboptimal initial condition is visualised in the accompanying figure 14(*b*). We observe that the suboptimal flow structure is exclusively located in the near-corner region with a spanwise extent similar to the corner mode. This observation is remarkable, considering that $> 90\,\%$ of the contributing modes, i.e. all even symmetric Tollmien–Schlichting modes, possess strong non-decaying spatial support along both walls up to the far field. Seemingly,

https://doi.org/10.1017/jfm.2014.31 Published online by Cambridge University Press

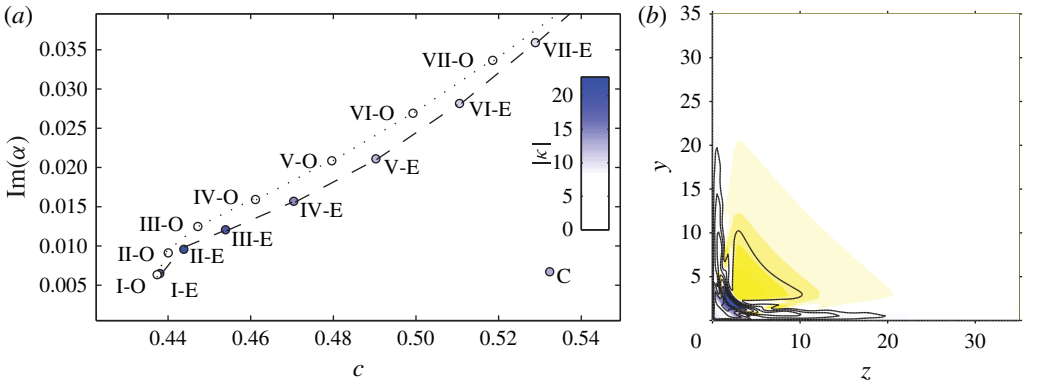


FIGURE 14. Optimal spatial initial condition for $Re_x = 57\,500$ and $\omega = 0.13$: (*a*) spectrum indicating the amplitude $|\kappa|$ of the modal expansion coefficients; (*b*) spatial structure visualised as in figure 4.

the complex expansion coefficients are optimised in such a way that destructive wave interference leads to localisation in the near-corner region.

In order to shed some light on the role of specific modes in the expansions, the corresponding modes are excluded in reduced subspaces, and the resulting energy gain curves are compared in figure 15(*a*). Figure 15(*b–d*) depict the spectra of the full subspace, the reduced subspace with the leading mode II-E removed, and the reduced subspace with the corner mode C removed, respectively. The expansion coefficient moduli are indicated as in figure 14(*a*). Per definition, the overall maximum energy gain is achieved for the non-reduced subspace of 30 modes. From figure 15(*c*) and the corresponding energy gain curve in figure 15(*a*), no qualitative difference can be seen when the leading mode is removed. The expansion coefficient amplitude gets redistributed among the other even viscous modes, and the maximum gain attained is somewhat lower. If, however, the corner mode is removed, then the gain decreases monotonically, and no transient energy amplification is observed. It is hence concluded that the corner mode plays a catalytic role in the expansion: no transient energy gain is possible if the mode is excluded from the expansion, whereas the occurrence of transient growth is not dependent on a full set of viscous modes. In conclusion, the spatial energy amplification can be regarded as the result of a viscid–inviscid interaction. This observation is also in agreement with the energetic analysis, where inviscid and viscid stability characteristics were associated with different parts of the Λ structure (compare figure 11(*a*,*b*), respectively).

The response corresponding to the suboptimal expansion at the streamwise location of maximum gain is visualised in figure 16(*a*). Figure 16(*b*) shows a three-dimensional reconstruction of the same local solution for comparison with the global mode of the same frequency from the direct simulation (§ 4.1), i.e. figure 7(*c*). Apparently, the suboptimal response closely resembles the Λ structure seen in the simulation results.

A quantitative comparison between non-modal theory and the numerical simulation is presented in figure 17 by means of modal amplification curves. The streamwise origin of the local analysis is moved to the neutral point position of the simulation data (same as shown in figure 9*a*). A good agreement between non-modal theory and numerical data in terms of the streamwise maxima's location and the relative offset of the curves is observed for $\omega \in [0.13, 0.19]$. For lower values of ω, however, the

https://doi.org/10.1017/jfm.2014.31 Published online by Cambridge University Press

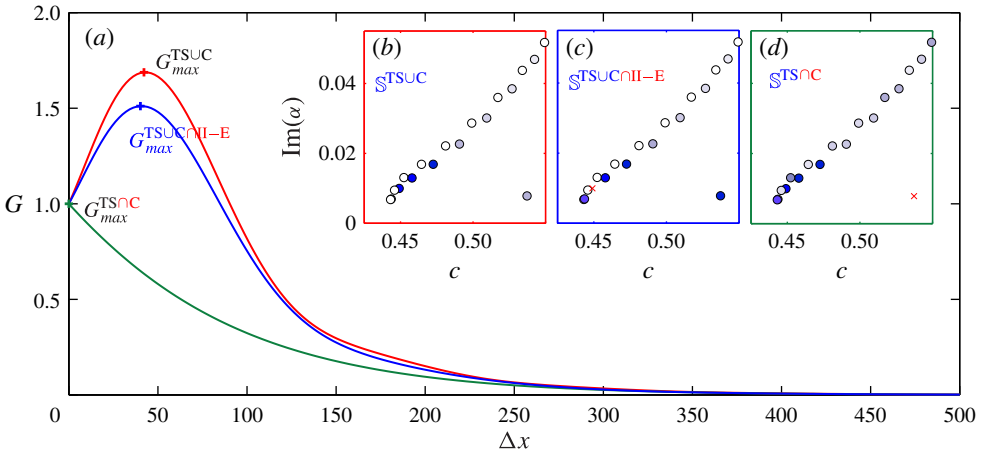


FIGURE 15. Spatial transient growth for different choices of eigenvector bases for $\omega = 0.13$ and $Re_x = 57\,500$. (*a*) Curves of the transient energy growth $G^{\mathbb{S}}$. (*b–d*) Corresponding spectra in: (*b*) full subspace consisting of the 29 leading TS modes and the corner mode (denoted $\mathbb{S}^{TS\cup C}$; red line in (*a*)); (*c*) full subspace but mode II-E excluded (denoted $\mathbb{S}^{TS\cup C\cap II-E}$; blue line in (*a*)); and (*d*) full subspace but corner mode excluded (denoted $\mathbb{S}^{TS\cap C}$; green line in (*a*)). Excluded modes are marked with a red cross. The expansion coefficient amplitude $|\kappa|$ is indicated in panels (*b–d*) as in figure 14(*a*).

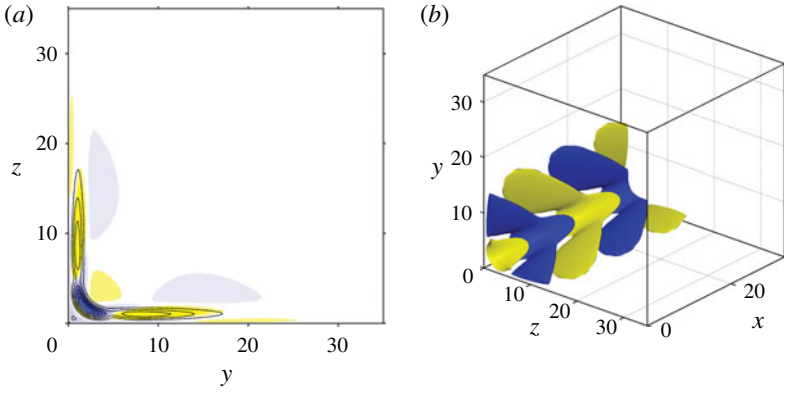


FIGURE 16. Optimal spatial response corresponding to the initial condition shown in figure 14: (*a*) spatial structure visualised as in figure 4; (*b*) three-dimensional reconstruction assuming parallel flow and zero spatial amplification visualised as in figure 7.

trend reverses and increasingly lower values of maximum gain are predicted by theory. It is noteworthy, though, that the deviation from the simulation occurs for $\omega \approx 0.11$, the same frequency as earlier identified as the separating value between two supposed mechanisms in the simulation (see figure 9*b*), and by the sensitivity analysis (see figure 13*c*). Obviously, the low-frequency mechanism cannot be represented by the eigenfunction expansion within the subset $\mathbb{S}^{TS\cup C}$. This is consistent with the analysis of the dependence of the resolvent norm on the frequency discussed in § 5.1.

https://doi.org/10.1017/jfm.2014.31 Published online by Cambridge University Press

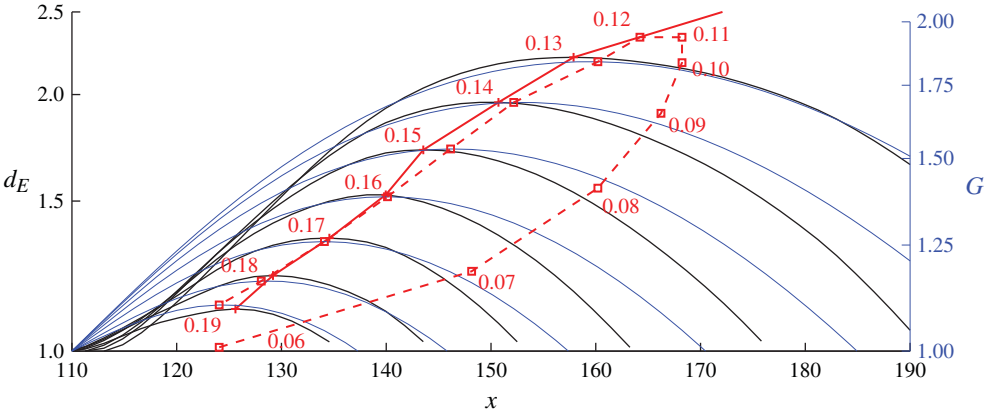


FIGURE 17. Comparison between energy density d_E (black full lines) from DNS results, and transient energy growth G (blue full lines) calculated at $Re_x = 57\,500$. The locations of the maxima in d_E (red full line with + signs) can be compared directly to the maxima of G (red dashed line with open squares). Curves are shown only for $\omega \in [0.13, 0.19]$ for clarity.

Note that the transient energy gain G in figure 17 is on a slightly different scale. In general, the non-modal approach underpredicts the simulation data by $\approx 20\,\%$. It has to be considered, though, that the approach is local, and therefore has a certain ambiguity in the choice of the Reynolds number for a convective problem. The results can be brought to very good agreement in terms of the positions of the maximum gains by slightly adjusting the Reynolds number. However, we wish to demonstrate that good agreement can be achieved even by taking the least biased choice, i.e. the middle of the computational domain. A possible explanation for the second mechanism, and reasons for why the eigenfunction expansion fails in this context, are addressed in appendix A.

6. Discussion and conclusions

The spatial stability of streamwise corner flow at $Ma = 0.8$ has been studied by means of linear stability theory, and compared to a DNS of the harmonically forced base state. Even though the flow is found to be subcritical by means of linear theory, frequency-dependant spatial amplification over some distance is observed behind the perturbation source in the DNS in the form of a Λ-shaped structure located in the near-corner region. A direct comparison of the results is enabled by spectrally decomposing the multi-frequency response of the simulated flow field by means of dynamic mode decomposition. The amplification behaviour suggests the presence of two distinct mechanisms that get mingled during the spatial downstream amplification process. This conjecture is further confirmed by a sensitivity analysis of the spatial linear stability operator, and quantitative agreement between the DNS results and local non-modal growth theory is achieved for the mechanism associated with higher frequencies. The corresponding spatial structure of the suboptimal response is also found in good visual agreement with the Λ structure observed in the DNS. In the low-frequency regime, the eigenvector expansion fails to predict correct amplification rates for numerical reasons detailed in appendix A. Despite these numerical issues, a highly likely scenario for the low-frequency mechanism is deduced from the numerical

https://doi.org/10.1017/jfm.2014.31 Published online by Cambridge University Press

evidence. It is further demonstrated that the inviscid corner mode plays a unique catalytic role in the spatial transient growth process. In conclusion, the subcritical amplification is identified as spatial transient growth through pseudo-resonance of viscous Tollmien–Schlichting waves with the inviscid corner mode. Beforehand, both inviscid and viscous characteristics are attested to the Λ structure by considering the modal perturbation energy balance.

Note that no optimal perturbation was specifically forced in the DNS, and yet spatial transient growth is observed and accurately predicted by theory. The present results are in agreement with the results of Alizard *et al.* (2013), where the authors calculated optimal perturbations for the incompressible corner flow solution under the parallel-flow assumption. The optimal structures found there compare well with the ones identified in the present study. Compare figure 19a,b in that reference with figures 4(*b*) and 16(*a*) of the present work, respectively. In their optimal temporal framework, Alizard *et al.* (2013) also identified two mechanisms that lead to a local and a global maximum in the temporal energy evolution.

It is found that physical insight into an instability mechanism can be gained by identifying the involved parts of the local linear stability spectrum through optimal expansions in the region of interest. The role of specific modes can also be examined by exclusion from the basis, as demonstrated for the corner mode in figure 15. The cooperation of two different types of global modes to form an optimal solution was also noticed by Garnaud *et al.* (2013) in a different context. Here, the authors found that the spatial structures associated with optimal body forcing inside the pipe of an incompressible configuration are built of a combination of local shear layer and jet column modes. As in our case, one mode is associated with a highly inflectional region, i.e. the shear layer in Garnaud *et al.* (2013), and the corner mode in ours. The weighting of the two mechanisms was found to be frequency-dependent, again, as in our case, and maximum transient growth was found for a combined scenario. This is a strong indication that viscid–inviscid pseudo-resonance might be a general phenomenon leading to selective noise amplification. This is also supported by the work of Alizard, Cherubini & Robinet (2009) where the authors investigated the sensitivity and optimal forcing in a laminar separation bubble. The latter flow shares the locally inflectional nature of streamwise corner flow, or the aforementioned jets, and reveals a similar tendency towards large transient growth through a pseudo-resonance. Seemingly, this particular kind of pseudo-resonance has to be expected whenever an inviscid and a viscid global structure spatially overlap. It would be desirable to test this conjecture further by considering other related flows such as the flow behind roughness elements, or over cavities and steps.

In ongoing work, the nonlinear behaviour of corner flow up to transition is examined by means of the same DNS set-up. The analysis of the stability characteristics in terms of an input–output analysis based on global singular modes in the spirit of Sipp & Marquet (2013) is numerically challenging, and also remains a future task.

Acknowledgements

The authors would like to thank J.-M. Chomaz for his valuable suggestions regarding spatial transient growth analysis, and the unknown referees for their insightful comments. Supercomputing time provided by the Federal High-Performance Computing Center Stuttgart (HLRS) under project LAMTUR is gratefully acknowledged. The project was supported by the Deutsche Forschungsgemeinschaft under grant RI 680/22.

https://doi.org/10.1017/jfm.2014.31 Published online by Cambridge University Press

Appendix A. Low-frequency transient amplification and limitations of the eigenfunction expansion

The discontinuity of the maximum resolvent's phase speed when ω is reduced in figure 13(c) suggests that a different or enlarged subset of eigenfunctions should be used to properly expand the low-frequency mechanism. Indeed, two likely candidates of discrete-mode branches are found close to the continuous branch in the full spectrum. The two branches consist of modes that are even and odd symmetric with respect to the bisector, and have spatial support around the latter. It is observed that these bisectorial modes get increasingly badly conditioned with increasing distance from the real axis. In general, it is found that ill-conditioned modes (often modes whose far-field behaviour is not properly represented by the boundary conditions) lead to non-physical transient amplification predictions when included in the eigenfunction expansion. As this is a rather numerical issue, it is addressed in appendix B. Transient growth calculations with the bisectorial mode branches included were conducted, and in fact do predict a second local maximum approximately at the anticipated streamwise locations. However, the energy gain is by far overpredicted, and the flow structures corresponding to the optimal initial condition and response exhibit maxima in the far-field corner. This indicates improper boundary conditions for the modes in question. In summary, the low-frequency transient amplification behaviour is likely to be described by the eigenfunction expansion including the bisectorial modes. However, the numerical techniques used for the present work do not allow for a proper representation of such modes, and hence the low-frequency transient growth. Please refer to appendix B for more details on eigenvector conditioning, and the connection with improper far-field boundary conditions for truncated modes.

Appendix B. Eigenvector conditioning of the spatial linear stability operator

In § 5.2, it became apparent that the inclusion of certain eigenfunctions in the expansion (2.24) leads to non-physical transient growth predictions. In the following, we connect the latter observation to the conditioning of eigenvectors, and to the far-field boundary representation, as well as domain truncation. The condition number of a simple eigenvalue α_i is given as

$$\varsigma = \frac{\tilde{\boldsymbol{p}}_i^H \tilde{\boldsymbol{q}}_i}{\|\tilde{\boldsymbol{p}}_i\|_2 \|\tilde{\boldsymbol{q}}_i\|_2} = \frac{1}{|\cos\theta_i|}, \tag{B 1}$$

where θ_i is the angle between a right eigenvalue $\tilde{\boldsymbol{q}}_i$ and a left eigenvalue $\tilde{\boldsymbol{p}}_i$ of $-\widetilde{\boldsymbol{M}}^{-1}\widetilde{\boldsymbol{L}}$. The interpretation is that perturbation of $O(\varepsilon)$ can cause a perturbation of $O(\varepsilon/|\cos\theta|)$ in the eigenvalue α. The discretised linear spatial stability operator $-\widetilde{\boldsymbol{M}}^{-1}\widetilde{\boldsymbol{L}}\tilde{\boldsymbol{q}} = \alpha\tilde{\boldsymbol{q}}$ results from the reduction of the generalised eigenvalue problem (2.20) to a standard one, and requires the inversion of $\widetilde{\boldsymbol{M}}$. The condition number ς is calculated for the full set of eigenvectors obtained by means of the QR algorithm for $\omega = 0.19$ and $\omega = 0.06$, representing the high- and the low-frequency regime, respectively. In figure 18, the condition number is indicated in the corresponding spectra. The highest values referring to the most ill-conditioned eigenvectors are found for the modes close to the real axis at unity phase velocity, i.e. continuous modes of a high spanwise wavelength. In general, the homogeneous Neumann boundary conditions do not represent the two-dimensional wave structure of such modes sufficiently, and lead to maxima of the eigenvector along the far-field boundaries. This effect gets more pronounced with increasing spanwise wavelength. For the same reason, the corner

https://doi.org/10.1017/jfm.2014.31 Published online by Cambridge University Press

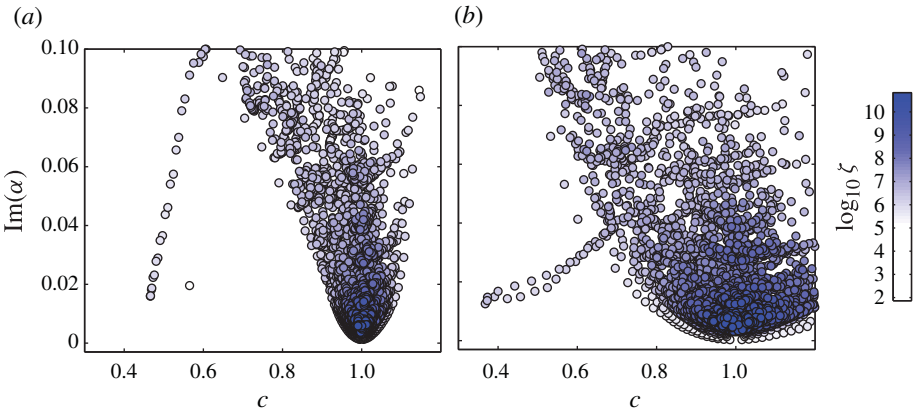


FIGURE 18. Spectra showing the eigenvalue condition number ς of the spatial linear stability matrix $-\widetilde{\boldsymbol{M}}^{-1}\widetilde{\boldsymbol{L}}$ at $Re_x = 57\,500$ for (*a*) $\omega = 0.19$ and (*b*) $\omega = 0.06$.

mode is the best conditioned mode in figure 18(*a*) since it has compact support, and is hence not influenced by the far-field conditions. In figure 18(*b*), the two parabola-shaped branches of bisectorial modes are readily identifiable as they enclose the continuous spectrum. This class of modes is favourably conditioned close to the real axis. Here, the modes' spatial extent is limited to the region close to the corner, whereas their bisectorial extent increases further upwards in the spectrum, and results in inferior conditioning. The latter ill-conditioned modes exhibit numerical artefacts in the far-field corner region, and prohibit a successful eigenvector expansion of the low-frequency transient growth mechanism. In this case, it is no longer possible to distinguish between numerical error and physical transient growth.

REFERENCES

ALIZARD, F., CHERUBINI, S. & ROBINET, J.-C. 2009 Sensitivity and optimal forcing response in separated boundary layer flows. *Phys. Fluids* **21** (6), 064108.

ALIZARD, F., ROBINET, J.-C. & GUIHO, F. 2013 Transient growth in a right-angled streamwise corner. *Eur. J. Mech. Fluids* **37**, 99–111.

ALIZARD, F., ROBINET, J.-C. & RIST, U. 2010 Sensitivity analysis of a streamwise corner flow. *Phys. Fluids* **22** (1), 014103.

BABUCKE, A. 2009 Direct numerical simulation of noise-generation mechanisms in the mixing layer of a jet. PhD thesis, Universität Stuttgart.

BABUCKE, A., KLOKER, M. J. & RIST, U. 2008 DNS of a plane mixing layer for the investigation of sound generation mechanisms. *Comput. Fluids* **37** (4), 360–368.

BAGHERI, S. 2013 Koopman-mode decomposition of the cylinder wake. *J. Fluid Mech.* **726**, 596–623.

BALACHANDAR, S. & MALIK, M. R. 1995 Inviscid instability of streamwise corner flow. *J. Fluid Mech.* **282**, 187–201.

BARCLAY, W. H. 1973 Experimental investigation of the laminar flow along a straight 135-deg corner. *Aeronaut. Q.* **24**, 147–154.

BARCLAY, W. H. & EL-GAMAL, H. A. 1983 Streamwise corner flow with wall suction. *AIAA J.* **21**, 31–37.

BARCLAY, W. H. & EL-GAMAL, H. A. 1984 Further solutions in streamwise corner flow with wall suction. *AIAA J.* **22**, 1169–1171.

https://doi.org/10.1017/jfm.2014.31 Published online by Cambridge University Press

BARCLAY, W. H. & RIDHA, A. H. 1980 Flow in streamwise corners of arbitrary angle. *AIAA J.* **18**, 1413–1420.

CARRIER, G. 1947 The boundary layer in a corner. *Q. Appl. Maths* **4**, 367–370.

CHEN, K. K., TU, J. H. & ROWLEY, C. W. 2011 Variants of dynamic mode decomposition: boundary condition, Koopman, and Fourier analyses. *J. Nonlinear Sci.* **22** (6), 887–915.

CHOMAZ, J.-M. 2005 Global instabilities in spatially developing flows: non-normality and nonlinearity. *Annu. Rev. Fluid Mech.* **37**, 357–392.

CHU, B.-T. On the energy transfer to small disturbances in fluid flow (Part I). *Acta Mechanica* **1** (3), 215–234.

DHANAK, M. R. 1992 Instability of flow in a streamwise corner. *ICASE Report No.* 92-70. Institute for Computer Applications in Science and Engineering, NASA Langley Research Center.

DHANAK, M. R. 1993 On the instability of flow in a streamwise corner. *Proc. R. Soc. Lond.* A **441**, 201–210.

DHANAK, M. R. & DUCK, P. W. 1997 The effects of freestream pressure gradient on a corner boundary layer. *Proc. R. Soc. Lond.* A **453** (1964), 1793–1815.

DRAZIN, P. G. & REID, W. H. 2004 *Hydrodynamic Stability*. Cambridge University Press.

DUCK, P. W., STOW, S. R. & DHANAK, M. R. 1999 Non-similarity solutions to the corner boundary-layer equations (and the effects of wall transpiration). *J. Fluid Mech.* **400**, 125–162.

EL-GAMAL, H. A. & BARCLAY, W. H. 1978 Experiments on the laminar flow in a rectangular streamwise corner. *Aeronaut. Q.* **29**, 75–97.

FARRELL, B. F. 1988 Optimal excitation of perturbations in viscous shear flow. *Phys. Fluids* **31**, 2093–2102.

GALIONIS, I. & HALL, P. 2005 Spatial stability of the incompressible corner flow. *Theor. Comput. Fluid Dyn.* **19**, 77–113.

GARNAUD, X., LESSHAFFT, L., SCHMID, P. J. & HUERRE, P. 2013 The preferred mode of incompressible jets: linear frequency response analysis. *J. Fluid Mech.* **716**, 189–202.

GASTER, M. 1962 A note on the relation between temporally-increasing and spatially-increasing disturbances in hydrodynamic stability. *J. Fluid Mech.* **14** (2), 222–224.

GHIA, K. N. & DAVIS, R. T. 1974 A study of compressible potential and asymptotic viscous flows for corner region. *AIAA J.* **12**, 355–359.

HANIFI, A., SCHMID, P. J. & HENNINGSON, D. S. 1996 Transient growth in compressible boundary layer flow. *Phys. Fluids* **8**, 826–837.

KLOKER, M. J. 1997 A robust high-resolution split-type compact FD scheme for spatial direct numerical simulation of boundary-layer transition. *Appl. Sci. Res.* **59** (4), 353–377.

KORNILOV, V. I. & KHARITONOV, A. M. 1982 On the part played by the local pressure gradient in forming the flow in a corner. *Fluid Dyn.* **17**, 242–246.

LAKIN, W. D. & HUSSAINI, M. Y. 1984 Stability of the laminar boundary layer in a streamwise corner. *Proc. R. Soc. Lond.* A **393**, 101–116.

LIN, R. S., WANG, W. P. & MALIK, M. R. 1996 Linear stability of incompressible viscous flow along a corner. In *Boundary Layer and Free Shear Flows: Proceedings of the ASME Fluids Engineering Division, Summer Meeting* vol. 237, pp. 633–638.

MACK, L. M. 1984 *Boundary-Layer Linear Stability Theory*. *(AGARD Special Course on Stability and Transition of Laminar Flow)*.

MIKHAIL, A. G. & GHIA, K. N. 1978 Viscous compressible flow in the boundary region of an axial corner. *AIAA J.* **16**, 931–939.

MORKOVIN, M. V., RESHOTKO, E. & HERBERT, T. 1994 Transition in open flow systems – a reassessment. *Bull. Am. Phys. Soc.* **39** (9), 1882.

NOMURA, Y. 1962 Theoretical and experimental investigations on the incompressible viscous flow around the corner. *Memo.* no. 2, pp. 115–145. Defence Academy of Japan.

PAL, A. & RUBIN, S. G. 1971 Asymptotic features of viscous flow along a corner. *Q. Appl. Maths* **29**, 91–108.

PARKER, S. J. & BALACHANDAR, S. 1999 Viscous and inviscid instabilities of flow along a streamwise corner. *Theor. Comput. Fluid Dyn.* **13**, 231–270.

https://doi.org/10.1017/jfm.2014.31 Published online by Cambridge University Press

REDDY, S. C., SCHMID, P. J. & HENNINGSON, D. S. 1993 Pseudospectra of the Orr–Sommerfeld operator. *SIAM J. Appl. Maths* **53** (1), 15–47.

RIDHA, A. 1992 On the dual solutions associated with boundary-layer equations in a corner. *J. Engng Maths* **26**, 525–537.

RIDHA, A. 2002 Combined free and forced convection in a corner. *Intl J. Heat Mass Transfer* **45** (10), 2191–2205.

RIST, U. & FASEL, H. 1995 Direct numerical simulation of controlled transition in a flat-plate boundary layer. *J. Fluid Mech.* **298**, 211–248.

ROWLEY, C. W., MEZIĆ, I., BAGHERI, S., SCHLATTER, P. & HENNINGSON, D. S. 2009 Spectral analysis of nonlinear flows. *J. Fluid Mech.* **641** (1), 115–127.

RUBIN, S. G. 1966 Incompressible flow along a corner. *J. Fluid Mech.* **26** (1), 97–110.

RUBIN, S. G. & GROSSMAN, B. 1971 Viscous flow along a corner: numerical solution of the corner layer equations. *Q. Appl. Maths* **29**, 169–186.

RUBIN, S. G. & TANNEHILL, J. C. 1992 Parabolized/reduced Navier–Stokes computational techniques. *Annu. Rev. Fluid Mech.* **24**, 117–144.

SCHMID, P. J. & HENNINGSON, D. S. 2001 *Stability and Transition in Shear Flows*. Springer.

SCHMID, P. J. 2010 Dynamic mode decomposition of numerical and experimental data. *J. Fluid Mech.* **656**, 5–28.

SCHMID, P. J. & HENNINGSON, P. J. 1994 Optimal energy density growth in Hagen–Poiseuille flow. *J. Fluid Mech.* **277**, 197–225.

SCHMIDT, O. T. & RIST, U. 2011 Linear stability of compressible flow in a streamwise corner. *J. Fluid Mech.* **688**, 569–590.

SIPP, D. & MARQUET, O. 2013 Characterization of noise amplifiers with global singular modes: the case of the leading-edge flat-plate boundary layer. *Theor. Comput. Fluid Dyn.* **27** (5), 617–635.

TANNEHILL, J., ANDERSON, D. & PLETCHER, R. 1997 *Computational Fluid Mechanics and Heat Transfer*. Taylor & Francis.

THEOFILIS, V. 2003 Advances in global linear instability analysis of nonparallel and three-dimensional flows. *Prog. Aerosp. Sci.* **39**, 249–315.

TREFETHEN, L. N. 1991 Pseudospectra of matrices. In *Numerical Analysis* (ed. D. F. Griffiths & G. A. Watson), pp. 234–266. Longman Scientific & Technical.

TREFETHEN, L. N., TREFETHEN, A. E., REDDY, S. C. & DRISCOLL, T. A. 1993 Hydrodynamic stability without eigenvalues. *Science* **261** (5121), 578–584.

TUMIN, A. & RESHOTKO, E. 2001 Spatial theory of optimal disturbances in boundary layers. *Phys. Fluids* **13** (7), 2097–2104.

WEINBERG, B. C. & RUBIN, S. G. 1972 Compressible corner flow. *J. Fluid Mech.* **56**, 753–774.

WRIGHT, T. G. 2002 Eigtool. Available at: http://www.comlab.ox.ac.uk/pseudospectra/eigtool/.

ZAMIR, M. 1981 Similarity and stability of the laminar boundary layer in a streamwise corner. *Proc. R. Soc. Lond.* A **377**, 269–288.

ZAMIR, M. & YOUNG, A. D. 1970 Experimental investigation of the boundary layer in a streamwise corner. *Aeronaut. Q.* **21**, 313–339.

ZAMIR, M. & YOUNG, A. D. 1979 Pressure gradient and leading edge effects on the corner boundary layer. *Aeronaut. Q.* **30**, 471–483.

https://doi.org/10.1017/jfm.2014.31 Published online by Cambridge University Press